

# Optical absorption and scattering spectroscopies of single nano-objects

Cite this: *Chem. Soc. Rev.*, 2014, 43, 3921

Aurélien Crut,\* Paolo Maioli, Natalia Del Fatti and Fabrice Vallée

Developments of optical detection and spectroscopy methods for single nano-objects are key advances for applications and fundamental understanding of the novel properties exhibited by nanosize systems. These methods are reviewed, focusing on far-field optical approaches based on light absorption and elastic scattering. The principles of the main linear and nonlinear methods are described and experimental results are illustrated in the case of metal nanoparticles, stressing the key role played by the object environment, such as the presence of a substrate, bound surface molecules or other nano-objects. Special attention is devoted to quantitative methods and correlation of the measured optical spectra of a nano-object with its morphology, characterized either optically or by electron microscopy, as this permits precise comparison with theoretical models. Application of these methods to optical detection and spectroscopy for single semiconductor nanowires and carbon nanotubes is also presented. Extension to ultrafast nonlinear extinction or scattering spectroscopies of single nano-objects is finally discussed in the context of investigation of their nonlinear optical response and their electronic, acoustic and thermal properties.

Received 16th October 2013

DOI: 10.1039/c3cs60367a

[www.rsc.org/csr](http://www.rsc.org/csr)

## 1. Introduction

The fast development of nanosciences and nanotechnology has been fostered both by technological requirements, *i.e.*, miniaturization of devices together with the increase of their functionalities, and by the novel or modified physical and chemical properties exhibited by nano-objects and nanomaterials.

FemtoNanoOptics Group, Institut Lumière Matière UMR5306, Université Lyon 1-CNRS, 69622 Villeurbanne, France. E-mail: aurelien.crut@univ-lyon1.fr



**Aurélien Crut**

*Institut Lumière Matière of University Lyon 1, specialized in optical investigations of nanomaterials. His present research is focused on the modeling of the optical and vibrational properties of nano-objects.*

These differ from those of the parent bulk materials in very different domains such as electronics, optics, magnetism, mechanics, thermics or catalysis. Controlled synthesis of nano-systems, and experimental investigation and theoretical modeling of their size-dependent properties are thus key challenges from both fundamental and technological points of view.

In this context, the optical response of nano-objects offers many opportunities for applications, and also for non-contact studies of their other properties<sup>1–4</sup> and of the impact of interaction with their environment (charge and energy exchanges,



**Paolo Maioli**

*spectroscopy of metal and hybrid nanoparticles, both through ensemble and single-particle experiments.*

local field enhancement effects).<sup>5–9</sup> The optical response of nano-objects is strongly affected by modifications of both the material electronic states due to quantum confinement, and the spatial distribution of the incident or emitted electromagnetic field in and around a nano-object (dielectric confinement). The former is dominant in semiconductor nanoparticles, as illustrated by the large size-dependence of the peak fluorescence wavelength of quantum dots,<sup>1</sup> very small metallic objects (with sizes typically below 2–3 nm) or carbon nanotubes. Quantum confinement effects play minor roles in larger size metal nano-objects. This difference results from the very high free electron density in metals ( $\sim 10^{22} \text{ cm}^{-3}$ ) compared with typical values in semiconductors.<sup>10</sup> In metallic media of nanometric size, electronic properties therefore stem from quantized states close to the Fermi level within the conduction band. The separations between these energy levels are very small compared with their widths and the thermal energy (at room temperature). For sufficiently large nanoparticles (size larger than typically 2 nm) these states can therefore be modelled by a quasi-continuum, similar to that in the bulk metals.<sup>11,12</sup> Their optical response is dominated by dielectric confinement (or plasmonic) effects, resulting in the appearance of additional resonances (localized surface plasmon resonances, SPRs) in their absorption and scattering spectra.<sup>13,14</sup> Quantum and dielectric confinements have been extensively studied from both the fundamental point of view and for applications in many domains including biological imaging<sup>15</sup> and sensing,<sup>16</sup> medical therapy,<sup>17</sup> data storage,<sup>18</sup> nonlinear photonic devices<sup>19</sup> or energy harvesting.<sup>20</sup> Linear and nonlinear optical spectroscopies have also been extensively used to analyze many properties of nano-systems such as electron confinement effects,<sup>1</sup> electronic interactions,<sup>3</sup> vibrational modes,<sup>2,21</sup> nano-magnetism,<sup>4</sup> acoustical<sup>7,22</sup> and thermal<sup>8,23</sup> energy exchanges, charge transfer,<sup>6</sup> etc.

The optical properties of ensembles of nano-objects have now been extensively studied, the first scientific investigation

of colloidal gold being reported by Faraday in 1857,<sup>24</sup> and classical modeling for nanospheres by Mie in 1908.<sup>25</sup> Though, with the advance of synthesis techniques and the better control of particle morphology, experimental optical studies on ensembles of nano-objects have provided much information, they are intrinsically affected by averaging effects due to dispersion of their internal (size, shape, structure, composition) and external (surface bound molecules, substrate, other nano-objects, etc.) characteristics. These hamper quantitative analysis and detailed modeling of the influence of these parameters on the measured properties, limitations that can be overcome by investigating individual nano-objects. This is particularly important for metal nanoparticles whose linear and nonlinear optical response around their localized surface plasmon resonance is strongly dependent on both their morphology and environment. Furthermore the possibility of optically addressing a single nano-object makes possible its use as an ultimate nanodevice. For instance, in the context of biological imaging, single-particle tracking is exploited to follow the dynamics of biologically relevant molecules.<sup>15,26</sup> Individual nano-objects can also be used for sensing their local environment, using either the environment-dependence of their physical properties, e.g., their optical response<sup>16,27</sup> or, for metal nanoparticles, the large local field effect associated to their SPR to enhance optical signals due to neighboring molecules (Raman scattering, fluorescence).<sup>9,28</sup>

Optical detection and spectroscopy of a single nanoscale system were first reported for a molecule by modulating the wavelength of the incident laser around one of its absorption lines, a method only applicable for spectrally narrow absorption resonances.<sup>29</sup> A simpler approach has been further developed based on detection of the fluorescence of a single photoexcited molecule, first at low temperature,<sup>30</sup> and subsequently at room-temperature, using either near-field<sup>31</sup> or far-field<sup>32</sup> optical microscopies. This method exploits high sensitivity detection of the



**Natalia Del Fatti**

*Natalia Del Fatti studied electronic engineering at Politecnico di Milano (Italy) and physics at Ecole Polytechnique (France), where she also received her PhD in 1999. She has more than fifteen years of experience in the field of ultrafast dynamics of semiconductors, bulk metals and metal nanoparticles. She was appointed Assistant Professor at the University of Bordeaux in 2000, where she developed a novel research axis on single*

*nano-object optical spectroscopy. Professor at University of Lyon 1 since 2006 and member of Institut Universitaire de France, she founded and leads the FemtoNanoOptics group. Her current research interests include nonlinear optics, ultrafast lasers, plasmonics and nanophysics.*



**Fabrice Vallée**

*After a degree in physics at Ecole Normale Supérieure (Paris) and a PhD from University Pierre et Marie Curie, Fabrice Vallée joined the CNRS in 1984. He worked at the Ecole Polytechnique on nonlinear optics, short pulse lasers and time-resolved spectroscopy of solids until 2000. He then created a new research group on nanophysics at the University of Bordeaux, and became Director of the CPMOH Institute in 2002. In 2007, he founded and leads the*

*FemtoNanoOptics group and is Director of the Fédération de Recherche Ampère in physics. His current research interests include nanosciences and nanotechnology, nonlinear optics, femtosecond lasers, and time-resolved optical spectroscopy.*

emitted light after its separation from the illuminating one by spectral filtering.<sup>33</sup> It was extended to individual fluorescent nano-objects, such as quantum dots or wires, or semiconducting carbon nanotubes, and is now a routine experiment for optical detection and spectroscopy of high quantum yield systems.<sup>33–37</sup> It was also recently demonstrated for weakly luminescent single nano-objects, such as plasmonic metal nanoparticles, taking advantage of the light emission enhancement by their surface plasmon resonance.<sup>38,39</sup>

Optical detection and spectroscopy of a single nano-object *via* detection of the direct signatures of its linear interactions with a light beam, *i.e.*, its elastic or inelastic scattering or absorption, or nonlinear ones (such as hyper-Rayleigh scattering or four-wave mixing),<sup>40–45</sup> have been only investigated during the last decade. Apart from yielding complementary information, as compared to luminescence spectroscopy, they also permit to address other objects, non-observable by luminescence, and to analyze different physical effects. They also open the way for selective investigation of nano-objects difficult to synthesize and present in minority in a sample (*e.g.*, dimers within a sample of mostly unpaired nano-objects<sup>46</sup>). They have also been at the origin of the development of ultrafast nonlinear scattering or extinction spectroscopies of single nano-objects, important tools for investigation of their other properties, such as their electronic, vibrational or thermal ones.<sup>47–54</sup>

In this paper, we review the main absorption- or scattering-based methods used for optical detection and spectroscopy of single nano-objects, focusing on the most commonly used techniques and excluding those exploiting fluorescence that have been reviewed elsewhere.<sup>33,55</sup> After presenting their general theoretical background, we focus on some commonly used setups as well as some promising recent developments, and introduce nonlinear optical methods. Their combination with a morphological characterization tool, *e.g.*, electron microscopy or atomic force microscopy, which represents an important advance for single nano-object studies, is also discussed. The information that can be obtained on the linear optical properties of individual nano-objects is mostly illustrated in the case of metal nanoparticles, focusing on quantitative comparison of the measured and computed optical spectra around their plasmonic resonance, and on the roles of the substrate and environment. Recent results on semiconductor quantum dots and nanowires as well as on carbon nanotubes are also briefly described. Finally, the ultrafast nonlinear optical absorption and scattering methods are described in the context of nonlinear plasmonics, as well as their exploitation in pump-probe spectroscopy to investigate ultrafast electron dynamics and acoustic vibrations of a single nano-object.

## 2. Single-particle detection and spectroscopy: absorption and scattering

Absorption- or scattering-based optical detection of a nano-object requires measurement of one of their relevant signal signatures in the near-field or far-field region. Though near-field methods have the key advantage of yielding information

on the local electromagnetic field distribution around the investigated object,<sup>56,57</sup> their applications have been limited by the difficulty of their interpretation (Section 2.2.1). This has fostered development of far-field methods. Their spatial resolution being limited by diffraction in the transverse direction to typically half of the light wavelength, and to typically one micron in the longitudinal one, optical observation of single nano-objects thus requires the use of thin very diluted samples. These usually consist of particles grown on a substrate (lithographed or chemically grown), or deposited on a substrate by spin-coating of a colloidal solution, or of thin films formed by nanoparticles embedded in a dielectric matrix. Linear interaction of these nano-objects with the incident light can be described *via* their absorption and scattering cross-sections, which depend on the composing material dielectric function and on the object internal and external characteristics. The detected optical signal depends on the illumination scheme (*e.g.*, plane wave, focused beam, evanescent wave *etc.*) but can be related to these cross-sections using general energy conservation considerations, as described below.<sup>58</sup>

### 2.1. Theoretical description of single-particle linear experiments

In the following, we consider typical illumination schemes: the ideal case of plane wave illumination of a nano-object in a homogeneous medium,<sup>58</sup> and its extension to more realistic experimental situations, by including focusing (*e.g.*, Gaussian beam illumination) and interface effects (*e.g.*, substrate-deposited nanoparticles).

When an incident electromagnetic field illuminates a nano-object embedded in a dielectric medium, the total electric field  $\mathbf{E}$  in the surrounding media is the sum of the incident,  $\mathbf{E}_i$ , and scattering ones,  $\mathbf{E}_{\text{scat}}$  (Fig. 1):

$$\mathbf{E} = \mathbf{E}_i + \mathbf{E}_{\text{scat}} \quad (1)$$

with a similar expression for the total magnetic field  $\mathbf{H} = \mathbf{H}_i + \mathbf{H}_{\text{scat}}$ . The scattered field generally consists in the superposition of evanescent and propagating waves. In the near-field region (distance smaller than the incident wavelength  $\lambda$  in the environment),  $\mathbf{E}_{\text{scat}}$  is dominated by evanescent waves. Conversely, in the far-field region (distance large as compared to  $\lambda$ ),  $\mathbf{E}_{\text{scat}}$  reduces to its propagating part. Describing the electromagnetic fields in complex notation,  $\mathbf{E}(\mathbf{r}, t) = \mathbf{E}(\mathbf{r})\exp(-i\omega t)$  (the real field being given by  $(\mathbf{E} + \mathbf{E}^*)/2$ ),  $\mathbf{E}_{\text{scat}}$  can then be written as:<sup>58</sup>

$$\mathbf{E}_{\text{scat}}(\mathbf{r}) = E_0 \frac{e^{ikr}}{-ikr} \mathbf{X}(\theta, \varphi) \quad (2)$$

where  $k = 2\pi/\lambda$ . The nano-object has been assumed to be positioned at the origin of the reference frame,  $\theta$  and  $\varphi$  are the spherical coordinate angles, and  $\mathbf{X}$  the vector scattering amplitude for an incident  $x$ -polarized wave (with  $\mathbf{X}(\theta, \varphi) \cdot \mathbf{e}_r = 0$ ). The rate of electromagnetic energy flow is given by the time-averaged Poynting vector,  $\mathbf{S}$ , which can be decomposed into three contributions (Fig. 1):

$$\mathbf{S} = \frac{1}{2} \operatorname{Re}(\mathbf{E} \times \mathbf{H}^*) = \mathbf{S}_i + \mathbf{S}_{\text{scat}} + \mathbf{S}_{\text{ext}} \quad (3)$$

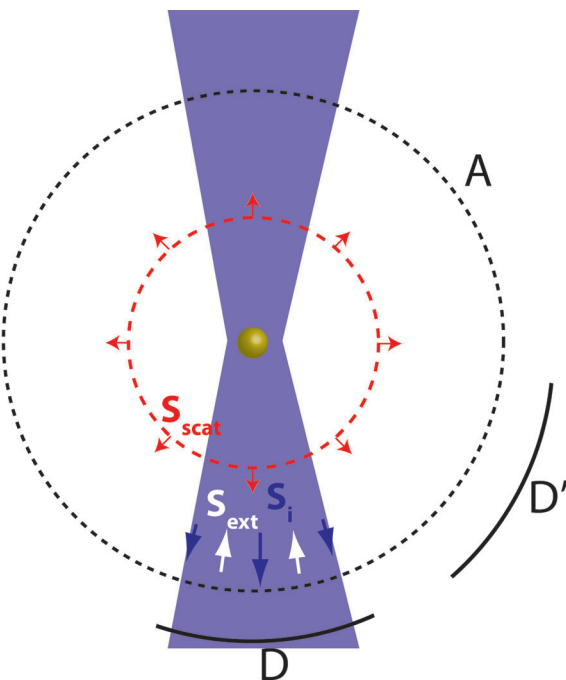


Fig. 1 Energy flows in single-particle experiments: illumination of a nanoparticle by an incident beam (Poynting vector  $\mathbf{S}_i$ ) leads to a scattered field (Poynting vector  $\mathbf{S}_{\text{scat}}$ ), whose interference with the incident field leads to extinction (Poynting vector  $\mathbf{S}_{\text{ext}}$ ). In the main text, energy balances are performed on an arbitrary closed surface A surrounding the nano-object, as well as on the area of a photodetector ( $D$  or  $D'$ ). In extinction-based measurements, the latter intercepts the incident beam ( $D$ ), while being positioned away from it in scattering-based approaches ( $D'$ ).

with

$$\begin{cases} \mathbf{S}_i = \frac{1}{2} \operatorname{Re}(\mathbf{E}_i \times \mathbf{H}_i^*) \\ \mathbf{S}_{\text{scat}} = \frac{1}{2} \operatorname{Re}(\mathbf{E}_{\text{scat}} \times \mathbf{H}_{\text{scat}}^*) \\ \mathbf{S}_{\text{ext}} = \frac{1}{2} \operatorname{Re}(\mathbf{E}_i \times \mathbf{H}_{\text{scat}}^* + \mathbf{E}_{\text{scat}} \times \mathbf{H}_i^*) \end{cases} \quad (4)$$

Assuming the medium embedding the nano-object is non-absorbing, the electromagnetic power  $P_{\text{abs}}$  absorbed by the object is given by (with a minus sign) the flux of  $\mathbf{S}$  through a closed surface  $A$  surrounding it (Fig. 1). As the flux associated to  $\mathbf{S}_i$  then vanishes, using eqn (3), this leads to:

$$P_{\text{ext}} = P_{\text{abs}} + P_{\text{scat}} \quad (5)$$

with

$$\begin{cases} P_{\text{abs}} = - \oint_A \mathbf{S} \cdot \mathbf{n} dS \\ P_{\text{scat}} = \oint_A \mathbf{S}_{\text{scat}} \cdot \mathbf{n} dS = \frac{|E_0|^2}{2\mu_0\omega k} \oint_A |\mathbf{X}(\theta, \varphi)|^2 \sin \theta d\theta d\varphi \\ P_{\text{ext}} = - \oint_A \mathbf{S}_{\text{ext}} \cdot \mathbf{n} dS \end{cases} \quad (6)$$

$P_{\text{scat}}$  is the total power scattered by the nano-object (the second equality being valid for  $A$  in the far-field region).  $P_{\text{ext}}$  is the total power extinction due to both absorption and scattering.

It reflects the flux of  $\mathbf{S}_{\text{ext}}$ , and is thus associated to interferences between the incident and scattered fields (eqn (4)).

In most experiments, a photodetector collects the light in a given direction over an area  $D$  (Fig. 1). Similarly, the detected far-field power  $P_d = \iint_D \mathbf{S} \cdot \mathbf{n} dS$  is the sum of three terms:

$$P_d = P_0 - P_e + P_s \quad (7)$$

with

$$\begin{cases} P_0 = \iint_D \mathbf{S}_i \cdot \mathbf{n} dS \\ P_s = \iint_D \mathbf{S}_{\text{scat}} \cdot \mathbf{n} dS = \frac{|E_0|^2}{2\mu_0\omega k} \iint_D |\mathbf{X}(\theta, \varphi)|^2 \sin \theta d\theta d\varphi \\ P_e = - \iint_D \mathbf{S}_{\text{ext}} \cdot \mathbf{n} dS \end{cases} \quad (8)$$

$P_0$  is the incident power, *i.e.*, measured in the absence of nanoparticles in the detection direction, and  $P_s$  is the scattered power collected by the detector.  $P_e$  is related to the nano-object extinction, and is identical to  $P_{\text{ext}}$  if the detector area is large enough to fully collect the incident light. As  $P_0$ , it vanishes if the detector is placed away from the incident beam.

The signature of the presence of a nano-object in the detected power is connected to the extinction ( $P_e$ ) and scattering ( $P_s$ ) contributions (eqn (7)). Obviously, their relative amplitudes strongly depend on the detection direction and on the nano-object size (scattering being much smaller than absorption for small nano-objects).<sup>14,58–60</sup> Scattering can be selectively detected if the detector is away from the incident beam (*i.e.*,  $P_0 = P_e = 0$  in eqn (7)),  $P_d$  then reducing to  $P_s$ , a fraction of the total scattered power  $P_{\text{scat}}$  (Fig. 1). This is related to the scattering cross-section  $\sigma_{\text{scat}}$  (with  $\sigma_{\text{scat}} = P_{\text{scat}}/I_0$ , for an incident plane wave of intensity  $I_0$ ), but, as the proportionality factor depends on the direction and angular acceptance of the detector and on the scattering diagram of the investigated object (also taking into account the presence of the substrate), quantitative determination of  $\sigma_{\text{scat}}$  in these experiments is not straightforward.

The situation is simpler in extinction-based measurements where the detector is in the forward direction and the incident beam is fully recollected ( $P_e = P_{\text{ext}}$ , see Fig. 1). The presence of a nanoparticle results in a decrease of  $P_d$  by  $P_{\text{ext}} - P_s$ , as compared to  $P_0$ . For an incident plane wave on a nano-object in a homogeneous medium, the power reduction (eqn (7)) is approximated by:<sup>58</sup>

$$P_{\text{ext}} - P_s \approx I_0 \frac{4\pi}{k^2} \operatorname{Re}(\mathbf{X}(\theta = 0) \cdot \mathbf{e}_x) - I_0 \Omega \frac{|\mathbf{X}(\theta = 0)|^2}{k^2} \quad (9)$$

where  $\Omega$  is the detector solid angle aperture centered about the forward direction.  $P_{\text{ext}}$  (and hence the extinction cross-section  $\sigma_{\text{ext}}$ ) is related to the light amplitude scattered in the forward direction,  $\theta = 0$ . This reflects the fact that, in the far field region, interference of the incident and scattered fields yields a non-vanishing contribution only in this direction (Fig. 2a). For a small nanoparticle, the scattered field can be identified to that of a dipole at the particle center and described by the particle polarizability  $\alpha$ . Using eqn (2) and (9), one then obtains  $\sigma_{\text{ext}} = k \operatorname{Im}(\alpha)$ .<sup>58</sup>

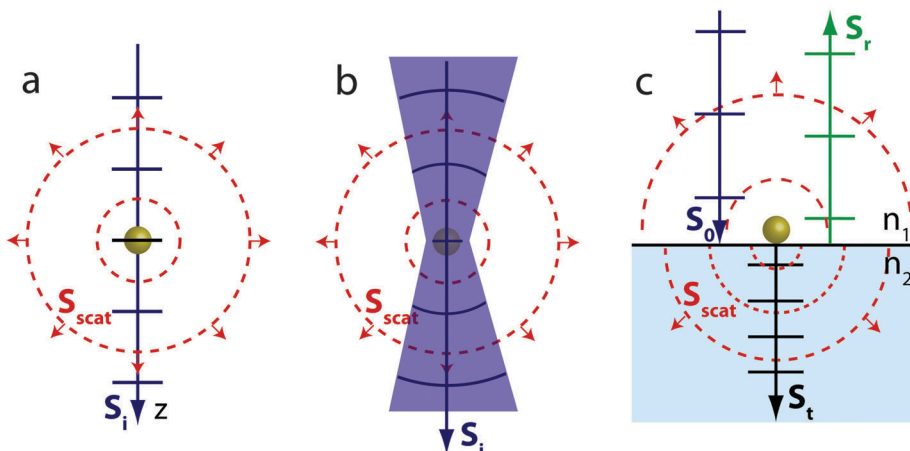


**Fig. 2** Wavefronts and energy flows of incident (blue lines) and scattered (red dashed lines) beams for (a) a plane wave and (b) a focused beam illuminating a nano-object (shown in yellow) in a homogeneous medium and (c) plane wave illumination of a nano-object deposited at the interface between two semi-infinite media with refractive indices  $n_1$  and  $n_2$  (only normal incidence on the interface was considered in the calculations). In the latter case, the incident field is separated into its initial (blue, subscript 0), reflected (green, subscript r) and transmitted (black, subscript t) components.

These results can be generalized to the case of an incident Gaussian beam (Fig. 2b) with small divergence  $\theta_0$  (beam aperture). In the far-field domain, the incident spherical wavefronts interfere with the scattered ones in the forward direction, and if the detector aperture  $\theta_{\max}$  (defining  $\Omega$ ) is equal to or larger than  $\theta_0$  (using for instance identical focusing and collecting lenses), the same expression as eqn (9) is obtained for the power reduction, where  $I_0$  is now the peak intensity of the Gaussian beam for a nano-object positioned at the center of the beam waist.

Most single-particle experiments were performed on nano-objects deposited on a dielectric substrate, providing them with an optically inhomogeneous environment (Fig. 2c). Typically, the substrate can either be much larger than the wavelength (*e.g.*, a glass slide) or smaller than it (*e.g.*, a 40 nm thick silica grid used for correlation with electron microscopy imaging). The presence of an interface modifies the excitation field experienced by the nanoparticle, as this results from the superposition of the incident and reflected ones, and also the particle scattering diagram (Fig. 3). This effect can be analytically analyzed in the simple case of a plane wave normally incident on an interface between two media of refractive indices  $n_1$  and  $n_2$ , with a small nano-object placed above it (Fig. 2c). Considering as a first approximation a purely dipolar response, the scattered field (eqn (2)) is then given by that radiated by a dipole in different environments in the forward and backward directions.<sup>61,62</sup> Extinction arises both in the forward direction (associated power  $P_{\text{ext},T}$ , due to interference between the transmitted and forward scattered fields), and in the backward direction ( $P_{\text{ext},R}$ , interference between the reflected and backward scattered fields). The total power lost by extinction in the two directions,  $P_{\text{ext}}$ , is then given by:

$$\begin{aligned} P_{\text{ext}} &= P_{\text{ext},T} + P_{\text{ext},R} = t^2 k_1 \text{Im}(\alpha) \\ P_{\text{ext},R}/P_{\text{ext},T} &= r/t \end{aligned} \quad (10)$$

where normal incidence Fresnel coefficients are given by  $r = (n_2 - n_1)/(n_1 + n_2)$  and  $t = 1 - r$ . For a homogeneous medium ( $n_1 = n_2$ ),  $P_{\text{ext}} = k_1 \text{Im}(\alpha)$  is recovered. In the case of weakly reflecting interfaces (with  $R = r^2 \ll 1$ ):

$$\begin{aligned} P_{\text{ext},T} &\approx P_{\text{ext}} = \sigma_{\text{ext}} I_0 \\ P_{\text{ext},R} &\approx \sqrt{R} \sigma_{\text{ext}} I_0 \end{aligned} \quad (11)$$

A similar analysis can be performed in the case of a thin substrate, where modifications of the scattering patterns due to the inhomogeneous environment are reduced (Fig. 3), but Fabry–Perot effects modify the reflected and transmitted fields.<sup>62</sup>

In the presence of an interface, the power measured locating a detector either on the transmitted or reflected path thus contains information on the particle extinction. In the case of a low reflectivity substrate, and small nanoparticles or sufficiently small angular collection, the collected scattered power can be neglected and extinction can be obtained from transmission measurements ( $P_d \approx P_0 - P_{\text{ext},T} \approx P_0 - P_{\text{ext}}$  as  $P_e = P_{\text{ext}} \gg P_s$ ). For larger nano-objects,  $P_s$  is not negligible anymore, and the measured power attenuation  $P_0 - P_d$  stands between  $P_{\text{abs}} = P_{\text{ext}} - P_{\text{scat}}$  and  $P_{\text{ext}}$ , depending on the nano-object scattering pattern (Fig. 3), and detector position and aperture. A similar approximation can be made in reflection, depending on the substrate reflectivity.

## 2.2. Single-particle linear optical techniques

Single-particle detection techniques in their linear version yield access to the scattered power ( $P_s$  in eqn (7)) or extinction-induced power change ( $P_e - P_s$  in eqn (7)), (absorbed power can be selectively detected by using a nonlinear approach, Section 2.3) (Table 1). These powers are usually much smaller than the incident one  $P_0$ , their selective detection requiring either spatial or temporal filtering, or large reduction of the fluctuations of  $P_0$ .

Spatial filtering is performed using a photodetector away from incident (or reflected) light beam direction (Fig. 1),

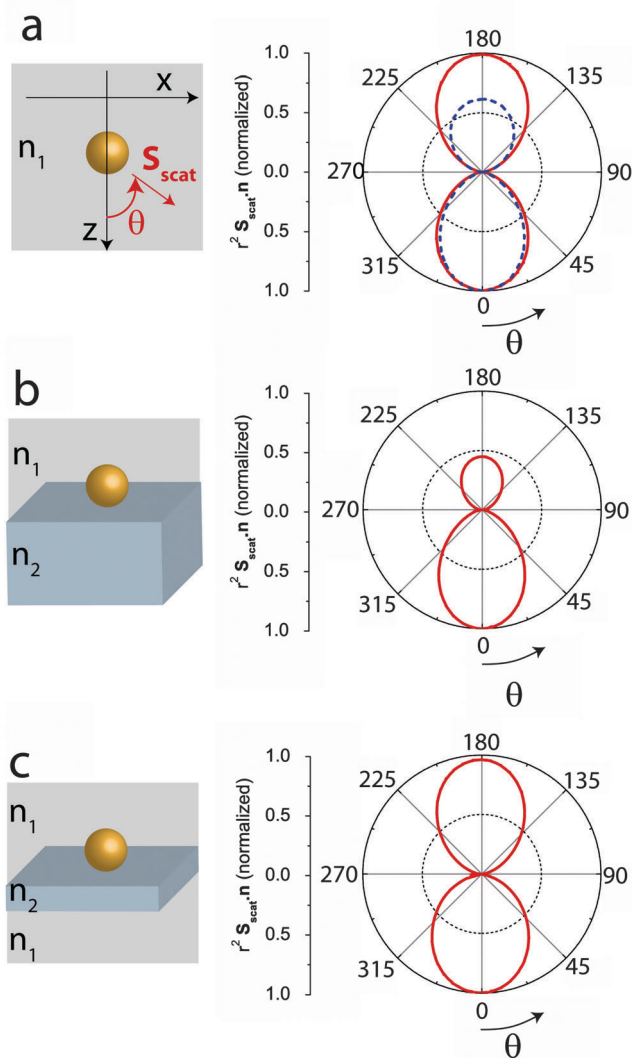


**Fig. 3** Scattering angular diagrams (red lines) of a 20 nm diameter gold nanosphere numerically computed using finite element modeling (FEM) at 510 nm, around its SPR wavelength, for different environments: (a) homogeneous with refractive index  $n_1 = 1$  (the scattering pattern of a 150 nm diameter sphere is shown for comparison, dashed blue line), and (b and c) at the interface between a medium of refractive index  $n_1 = 1$  and a semi-infinite (b) or a 20 nm thick (c) substrate of refractive index  $n_2 = 1.45$ .

yielding access to the scattered power in the detector direction (dark field microscopy, Section 2.2.2 and Table 1). As, in the small size regime, the scattering cross-section of nanoparticles scales as the square of their volume, the sensitivity of scattering methods is limited, and heterodyne methods have been developed to reduce the size detection threshold (Section 2.2.3). However, as the dominant optical response of a small size nano-object is its absorption (absorption cross-section scaling as the particle volume), methods based on measurement of its linear extinction have been developed to access it (Table 1).

Extinction-based methods are based on monitoring the beam power after its interaction with the object, either in the forward or backward direction (in the presence of a substrate).

Power changes relative to the transmitted or reflected light without nanoparticles are thus detected (eqn (7)). Though it has been recently achieved in a modulation-free approach permitting observation of a single dye molecule (using balanced photodetectors to reduce the sensitivity limit due to laser intensity fluctuations),<sup>63</sup> most methods rely on temporal modulation of the nano-object optical response, to discriminate it from the background transmitted or reflected light using lock-in detection (*e.g.*, to separate  $P_0$  and  $P_e - P_s$  in eqn (7)). The first modulation-based technique used modulation of the incident laser frequency around a strong absorption resonance of a single molecule, the resulting modulation of the observed extinction permitting its detection.<sup>29</sup> This method is however limited to narrow resonance systems and cannot be easily applied to metal or semiconductor nano-objects. Much simpler approaches are now used, modulating for instance nano-object position (spatial modulation spectroscopy,<sup>64,65</sup> Section 2.2.4, Table 1), or incident light polarization (polarization modulation microscopy,<sup>66</sup> Section 2.2.5). Though information on extinction is generally obtained, if the object is sufficiently small its scattering contribution can be neglected and the measured extinction can be identified to its absorption (which is typically the case for absorbing nano-objects with sizes below 30–50 nm, for instance  $\sigma_{\text{abs}}/\sigma_{\text{scat}} = 100$  and 1 for gold nanospheres with 20 nm and 80 nm diameters, respectively). After a brief description of near-field microscopy, in the following we will focus on discussions of these far-field techniques.

**2.2.1. Near-field microscopy.** Near-field methods exploit the nanoantenna effect, *i.e.*, conversion of evanescent into propagating waves (and *vice versa*). Their ability to detect single metal nanoparticles was demonstrated using the illumination mode of an aperture scanning near-field optical microscope (SNOM), the presence of a nanoparticle in the illuminated region (mostly *via* the evanescent field,  $E_i$ , at the SNOM tip) inducing radiation in the far-field domain (Fig. 4a, eqn (2)).<sup>67</sup> Information on the phase of the scattered light was obtained by analyzing its interference with the field emitted by the aperture, showing the phase shift occurring at the localized surface plasmon resonance of metal nanoparticles.<sup>68,69</sup> The nanoantenna effect was also used in the collection mode, light scattered in the near-field region by a nanoparticle illuminated by a far-field source being detected by the SNOM aperture.<sup>70</sup> Later experiments performed with apertureless SNOM (ASNOM)<sup>71</sup> permitted better spatial resolution and simultaneous topographical and optical characterization (Fig. 4b).<sup>72</sup> ASNOM operates with far-field illumination and detection, a nanoparticle being detected when it stands in the near-field region of the probe tip.<sup>57,73</sup>

The main advantage of SNOM techniques is their high spatial resolution and nanoscale field probing, which permits experimental mapping of the near-field around a nanoparticle, as demonstrated in the case of silver nanoprisms and gold nanodisks and nanorods.<sup>56,57,73,74</sup> The electromagnetic field distribution, a key parameter for many applications using local field enhancement around metallic nanoparticles, has been found to be mostly of dipolar and quadrupolar type for small and large nano-objects, respectively, in agreement with numerical simulations. However, interpretation of the measured spectra and

**Table 1** Main features of some of the most common far-field techniques for single particle detection and spectroscopy. The table summarizes the physical quantity measured by these techniques, the nature of the incident light beam, whether and how optical signals are temporally modulated, and the detection strategies for imaging and spectroscopy purposes. Additional information can be found in the main text

	Quantity measured	Light beam	Modulation	Detection
Dark-field microscopy (Section 2.2.2)	$\iint_D \frac{\partial \sigma_{\text{scat}}}{\partial \Omega} d\Omega$	Annular white lamp beam or total internal reflection	No	- Wide-field imaging on a CCD camera - Spectrometer
Spatial modulation spectroscopy (SMS) (Section 2.2.4)	$\sigma_{\text{ext}} - \iint_D \frac{\partial \sigma_{\text{scat}}}{\partial \Omega} d\Omega$	Focused laser or white lamp beam	Sample position relative to beam focal spot ( $f = 1.5$ kHz)	- Photodiode, lock-in detection at $f/2f$ - Imaging by sample scanning
Photothermal imaging (Section 2.3.2)	$\propto \sigma_{\text{abs}}$	Focused heating and probe beams	Heating beam intensity ( $f = 0.1\text{--}15$ MHz)	- Photodiode, lock-in detection at $f$ - Imaging by sample scanning

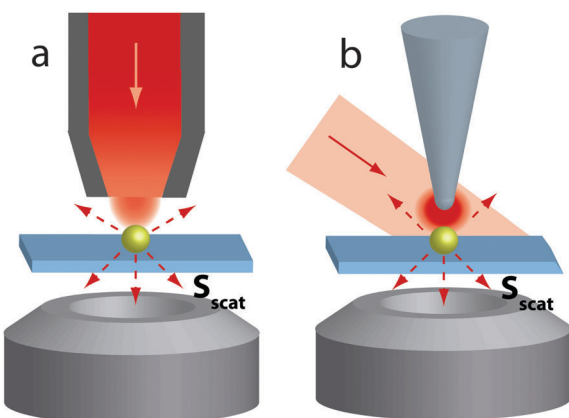


**Fig. 4** Schematic geometry of scanning near-field optical microscopy (SNOM) of a single nano-object: (a) aperture SNOM in illumination mode where the evanescent wave emerging from the tip is scattered by the object into far-field radiation (with  $S_{\text{scat}}$  the corresponding Poynting vector), part of which being collected by the detector. (b) Apertureless SNOM where the evanescent wave around the far-field illuminated object is scattered by a tip into the far-field.

collected light amplitude (*i.e.*, conversion of SNOM signals into optical cross-sections) is difficult, as it requires detailed modeling of the tip–nanoparticle optical interaction (actual tip geometry, electromagnetic field distribution at a probe tip, or alteration of the nano-object optical response due to the presence of the tip in its nanoscale environment).<sup>71,75,76</sup> These difficulties, together with the complexity of SNOM setups as compared to far-field ones, have limited their use in the context of single nanoparticle investigation.

**2.2.2. Dark-field scattering microscopy.** Dark-field microscopy is the most widely used optical tool for single-nanoparticle investigation.<sup>27,47,77–79</sup> It consists in selective collection of the scattered light, over a dark background, *i.e.*, in directions not illuminated by the incident field (Fig. 1), yielding access to a purely scattered power (given by  $P_s$  in eqn (7)). This is usually achieved by illuminating the sample with an annular beam and collecting the scattered light in a cone of smaller aperture than the incident beam (Fig. 5), or using evanescent wave excitation.<sup>80,81</sup> Associated to a broadly tunable light source such as a white lamp, spectral dispersion using a spectrometer and detection

on a CCD camera, the scattering spectra of single nano-objects can thus be straightforwardly measured over a large spectral range.<sup>78</sup> Because of this ease of operation and relatively fast acquisition time, dark field spectroscopy has been extensively applied to investigate many different types of nano-objects of different morphology and composition, such as metal and semiconductor nanoparticles, nanowires or nanotubes.<sup>47,77–79,82–84</sup> Furthermore the possibility of wide-field imaging has been exploited for single-particle tracking,<sup>85</sup> simultaneous monitoring of several individual nanoparticles using a CCD camera<sup>86,87</sup> or real time-monitoring of changes in nanoparticle morphology.<sup>88</sup>

Quantitative determination of the amplitude of the scattering cross-section  $\sigma_{\text{scat}}(\lambda)$  is more difficult, as the measured scattered light amplitude is proportional to the integral of the differential scattering cross-section over the collected area (eqn (8), with a factor that can be obtained by preliminary calibration<sup>89</sup>). Recovering the full scattering cross-section (eqn (6)) requires detailed description of the optical setup (excitation and collection angles<sup>90</sup>) and of the nano-object scattering diagram, which is affected by its size, shape and environment (such as the presence of a substrate, Fig. 3).<sup>89,91</sup> Moreover, the scattering cross-section of particles much smaller than the light wavelength decreases with the square of the particle volume  $V$  (the particle thus exhibiting a quasi-dipolar response), limiting the sensitivity of dark-field microscopy to nano-objects of few tens of nanometers (*e.g.*, about 20 nm and 30 nm for silver and gold nanospheres, respectively<sup>92,93</sup>).

**2.2.3. Homodyne and heterodyne techniques.** The nanoparticle size detection threshold can be reduced using homodyne or heterodyne techniques where the electromagnetic field,  $E_{\text{signal}}$ , to be detected interferes with a stronger reference field  $E_{\text{ref}}$ . The signal measured by a detector is then proportional to  $\text{Re}(E_{\text{signal}} E_{\text{ref}}^*)$ , and thus to the signal electric field, rather than to its square modulus.<sup>59</sup> For detection of the light scattered by small nanoparticles, it scales as  $V$  rather than  $V^2$  (eqn (2)), with, consequently, an improvement of particle size detection thresholds as compared to dark-field microscopy (however at the expense of experimental complexity).

This approach was implemented by detecting interference between light backscattered by a deposited nanoparticle and light reflected by the substrate.<sup>59</sup> Sensitivity is notably improved

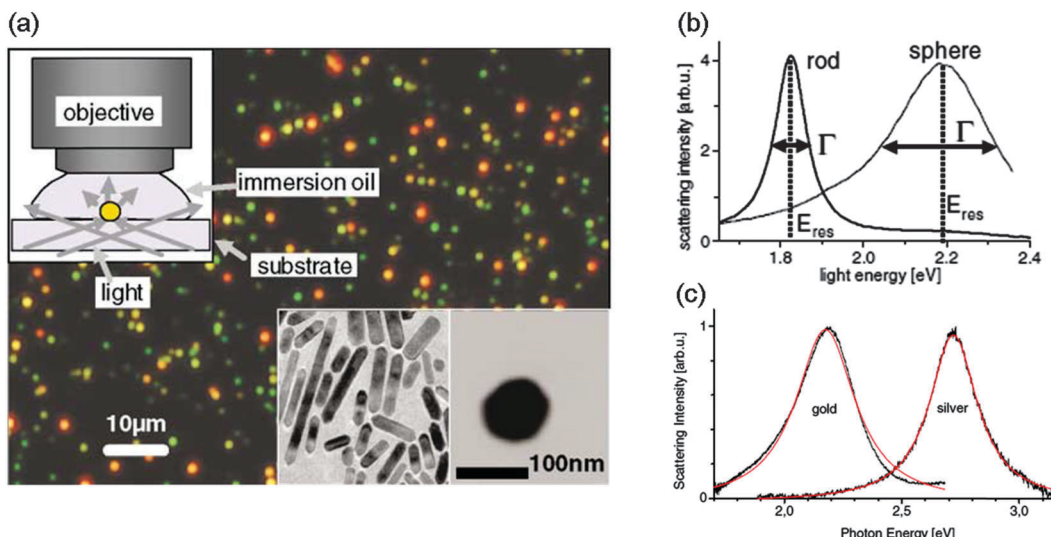


**Fig. 5** Dark-field microscopy. (a) Wide-field true color image of light scattered by single gold nanorods (red) and 60 nm gold nanospheres (green) on a substrate under far-field conical illumination (inset upper left). Transmission electron microscopy images of nano-objects from the same solution are shown at the bottom right.<sup>78</sup> Measured scattering spectra of one of these single rods and spheres (b),<sup>78</sup> and of gold and silver nanospheres with diameters of 60 nm (c).<sup>92</sup> Adapted with permission from ref. 78 (Copyright 2002 by The American Physical Society) and ref. 92 (Copyright IOP Publishing & Deutsche Physikalische Gesellschaft. CC BY-NC-SA).

as compared to the previously described scattering techniques, gold nanoparticles with diameters below 10 nm being identified (the measured spectra containing however competing size-dependent contributions from both particle scattering and absorption). Using an external reference beam instead of the reflected light, backscattering by a single particle in a liquid has been detected for single polystyrene and gold nanoparticles as small as 10 and 5 nm, respectively.<sup>94</sup> The accuracy of particle characterization and identification was later improved using a heterodyne scheme involving a slight frequency shift between scattered and reference fields to eliminate the background signals by lock-in detection.<sup>95</sup> Recently, scattering of the orthogonal polarization component (relative to the incident linear beam polarization) present in the focal plane of a tightly focused beam<sup>96</sup> has also been detected, permitting detection of 5 nm gold nanoparticles.<sup>97</sup>

An important interest of these techniques is that both the amplitude and phase of the detected field,  $E_{\text{signal}}$ , can be determined, yielding access to the polarizability of the investigated particle that fully describes its optical response (*i.e.*, its scattering and absorption).<sup>98</sup> This has been done using a scheme similar to that of differential interference contrast (DIC) microscopy, with two orthogonally polarized illuminating and reference beams focused on the sample with a spatial shift, and subsequently recombined by a Nomarski prism after the sample. Measuring signals proportional to  $|E_{\text{signal}} - E_{\text{ref}}|^2$  and  $|E_{\text{signal}} + E_{\text{ref}}|^2$ , the phase of the polarizability of gold nanoparticles in the 10–15 nm size range was directly obtained, its amplitude being however only indirectly determined after calibration through the response of dielectric nanoparticles.<sup>98</sup>

These techniques have been recently extended to 3D detection and localization of nanoparticles using digital heterodyne holography ( $\approx$  50 nm gold nanoparticles in water and biological

environments).<sup>99,100</sup> Its principle consists in recording a hologram resulting from the interferences between the scattered field and a reference one on a CCD camera, the full spatial information being coded in the holographic pattern (Fig. 6).<sup>101</sup> To increase the sensitivity, the reference and object beams are frequency-shifted by acousto-optic modulators, inducing a low-frequency beating of their interference pattern. A very promising aspect of this method is that it yields access to the amplitude and phase of the field scattered by a nanoparticle and to the angular scattering pattern from a single hologram, using numerical reconstruction algorithms.<sup>101–103</sup> Using radially and azimuthally polarized laser beam excitation in a confocal microscope, detection and mapping of the 3D orientation of individual gold nanorods in a polymer film was recently achieved. Information was extracted through concomitant acquisition of photoluminescence signals and homodyne detection of the scattered field.<sup>104</sup>

**2.2.4. Spatial modulation spectroscopy (SMS): extinction measurements.** A simple way to detect the extinction of light from a single nanoparticle is to modulate its position and detect the induced modulation of the transmitted power using a lock-in amplifier (Fig. 7).<sup>64</sup> Writing  $(x_0, y_0)$  the position in the focal plane of a nanoparticle much smaller than the beam size, and neglecting the recollected scattering light  $P_s$  in eqn (7) (an approximation whose accuracy increases for low aperture objectives and small nanoparticles, whose extinction is dominated by absorption), the measured signal is proportional to the extinction cross-section  $\sigma_{\text{ext}}(\lambda)$ :

$$P_0 - P_d \approx P_{\text{ext}} = \sigma_{\text{ext}} I(x_0, y_0 + \delta_y \sin(2\pi f t)) \quad (12)$$

where modulation is performed at frequency  $f$  along the  $y$  direction with an amplitude  $\delta_y$ .<sup>105</sup> Scanning the sample position and demodulating at frequencies  $f$  or  $2f$ , single nanoparticles

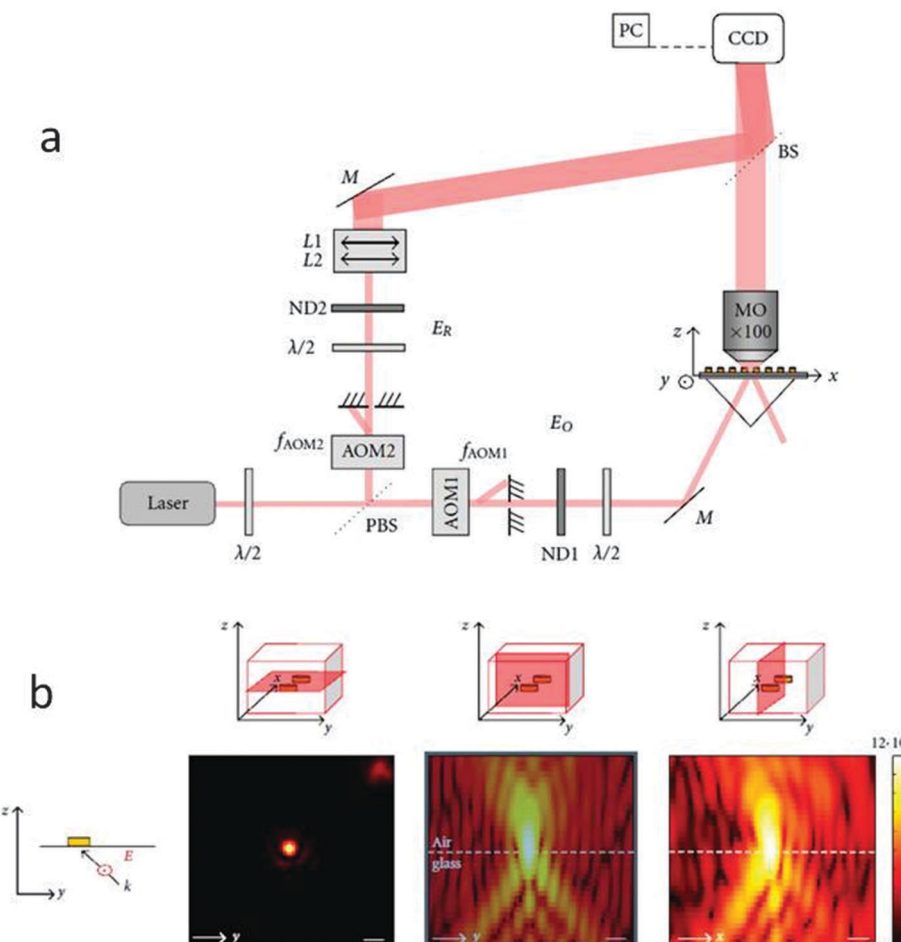


**Fig. 6** (a) Digital heterodyne off-axis holography setup showing the reference ( $E_R$ ) and object ( $E_O$ ) arms, acousto-optical modulator (AOM), (polarizing) beam splitter (P-BS), neutral density filters (ND), and microscope objective (MO) (see ref. 103 for details). (b) Intensity (arbitrary units) of the scattered field reconstructed from a single hologram at  $\lambda_{exc} = 785$  nm for a nanodisk dimer illuminated under *s*-polarized excitation. The scale bar corresponds to 1  $\mu$ m. Adapted from ref. 103.

lead to signals respectively proportional to first and second derivatives of the spatial intensity profile  $I$  with respect to the modulation direction, for small modulation amplitude (Fig. 7). SMS can also be performed by modulating the spot size position rather than the particle one, as recently shown for metal nano-objects and carbon nanotubes, with however a lower sensitivity due to technical difficulties in avoiding a spurious background from aperturing effects.<sup>106,107</sup>

The demodulated amplitude is directly proportional to the nano-object extinction cross-section  $\sigma_{ext}$  at the incident wavelength. Extinction spectra are then measured by varying the incident light wavelength using a tunable laser,<sup>46,108,109</sup> a supercontinuum source<sup>105,110</sup> or, as only a weak incident power is required, a white lamp.<sup>111</sup> As the detected signal is related to  $\sigma_{ext}$  through a proportionality factor depending only on measurable parameters (modulation amplitude and beam waist size), SMS provides the opportunity to determine the  $\sigma_{ext}$  absolute amplitude, *i.e.*, to fully characterize the extinction of a nano-object (Fig. 8). Using this approach, different single nano-objects have been detected and studied (Fig. 8), such as silver and gold

nanoparticles (as small as 5 nm), semiconductor nanowires, and single wall carbon nanotubes.<sup>64,109,112–114</sup> The limit of the method can be defined by the minimum  $\sigma_{ext}$  amplitude that can be detected, of the order of 2 nm<sup>2</sup>.<sup>64</sup> Like in dark-field microscopy, the light polarization dependent response of an object can be simply measured, changing the incident light polarization, and its 2D orientation (in the plane perpendicular to the incident beam direction) determined providing it exhibits an asymmetric optical response, as it is the case for nanorods (Fig. 8d) or nano-bipyramids.<sup>108</sup>

The SMS method measures the extinction of an object, and thus *a priori* contains information on both its scattering and absorption. These contributions can be separated retrieving the phase information using interferometric detection. This has been recently demonstrated by combining SMS with a common-path interferometer, illuminating the sample with two spatially shifted beams using a scheme similar to that of DIC microscopy (Fig. 9).<sup>106,115</sup>

A variant of transmission SMS, reflection spatial modulation spectroscopy (R-SMS) has been recently developed to investigate

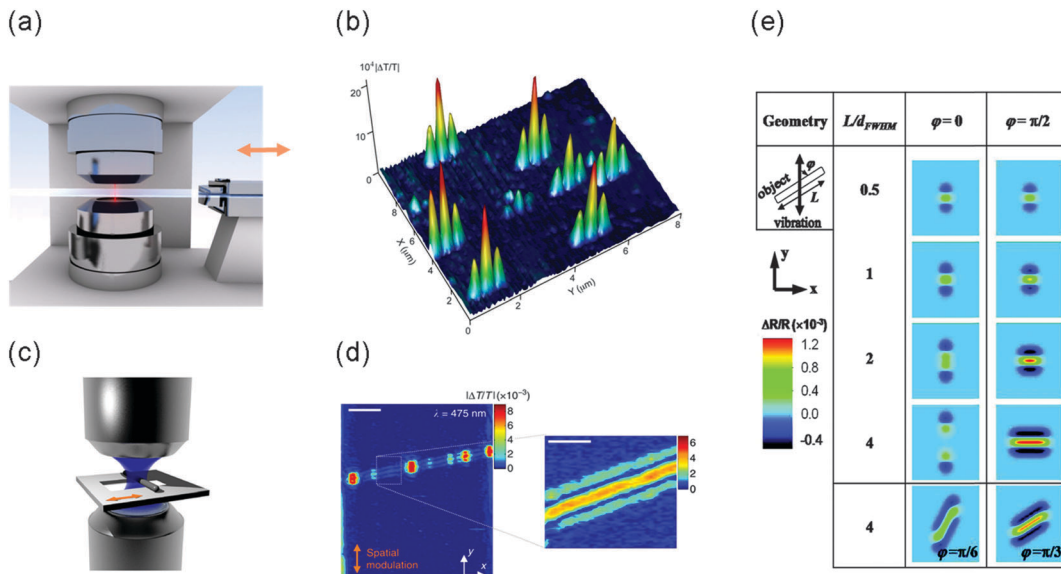


**Fig. 7** Spatial modulation spectroscopy (SMS) setup for linear optical extinction measurements (a and c), showing the focusing and collecting microscope objectives, with the substrate in between either supporting nano-objects with low density (less than one particle per  $\mu\text{m}^2$ ) (a) or nanowires or nanotubes over a trench (c). The sample is scanned in the  $x$ - $y$  directions, while a fast spatial modulation is applied along the  $y$  direction. (b) Relative power change ( $P_0 - P_d$ )/ $P_0$  (eqn (12)) measured by SMS at 530 nm,  $x$ - $y$  scanning the sample position over  $10 \times 8 \mu\text{m}^2$  for 15 nm diameter gold nanoparticles spin-coated on a glass substrate. Each single particle shows-up as a main peak with two satellites for the 2f demodulation used here. (d) SMS image of a suspended 1.83 nm single wall carbon nanotube for signal demodulation at frequency 2f. (e) Computed 2f R-SMS image of an absorbing elongated nano-object with an increasing aspect ratio, for different angles between the nano-object axis and the modulation direction. Adapted from ref. 65 (Copyright 2012 American Chemical Society) and ref. 116 (by permission from Macmillan Publishers Ltd: Nature Communications, copyright 2013).

single nano-objects deposited on an opaque substrate,<sup>65</sup> a frequent situation imposed by nanofabrication techniques or by the intended application of the fabricated nano-objects. Similar to the transmission geometry, the modulation amplitude of the reflected power can be quantitatively related to  $\sigma_{\text{ext}}$  (provided the recollected scattered power can be neglected), as demonstrated for single wall carbon nanotubes deposited on silica-on-silicon substrates.<sup>65,116</sup>

**2.2.5. Polarization modulation microscopy.** Another way of modulating the power  $P_d$  detected after light interaction with a nano-object is to modulate the linear polarization direction of the incident beam, provided the object's optical response exhibits a large dependence on light polarization. Modulation of the beam polarization is performed at high frequency (100 kHz) using a photoelastic modulator, and the light collected in the forward direction is detected and its modulated part measured using a lock-in amplifier.<sup>66</sup> As in SMS, the detected power depends on the nano-object extinction (neglecting the light scattered power  $P_s$  in the detector direction, eqn (7)), the demodulated signal amplitude being then proportional to the difference of extinction cross-sections for light polarized parallel and orthogonal to the nano-object axis. This technique has the advantage of a high modulation frequency (and thus reduced noise) but can be applied only to nano-objects with anisotropic shapes, such as nanorods, nanowires, or nanotubes.

### 2.3. Single-particle nonlinear optical techniques

The linear methods described above permit detection of single nano-objects and yield access to their scattering or

extinction response. Their absorption can be selectively addressed only if the object is sufficiently small to neglect the scattering contribution to extinction, and thus to identify extinction with absorption. Detection can also be performed using nonlinear spectroscopies, such as second or third order hyper-Rayleigh scattering, pump-probe spectroscopy (Kerr-like effect), or four-wave mixing. These can provide additional information on the linear response (*i.e.*, absorption) or the nonlinear optical polarizability of a single nano-object. The most commonly used methods are briefly described in the following.

**2.3.1. Photothermal techniques.** One of the most common ways of detecting a single absorbing nano-object is the photothermal method, which relies on thermally-mediated nonlinear optical interaction between two optical beams. The nano-object and its environment are periodically heated by a modulated beam, and the thermally induced modulation of the optical properties is detected by a probe beam focused at the same position. More precisely, when an absorbing nanoparticle is in the modulated heating beam focal spot, the particle and, by thermal diffusion, its environment, are periodically heated up. A periodic change of the refractive index in and around the particle is thus induced. This Kerr-like thermal effect results in periodic variations of the probe beam transmission or reflection at the heating modulation frequency, which can be extracted using lock-in detection. At the lowest order, the signal amplitude is proportional to the induced temperature modulation and thus to the nano-object absorption, with no contribution from scattering, an important advantage for particle detection in highly scattering environments as required for biological imaging applications.<sup>117,118</sup>

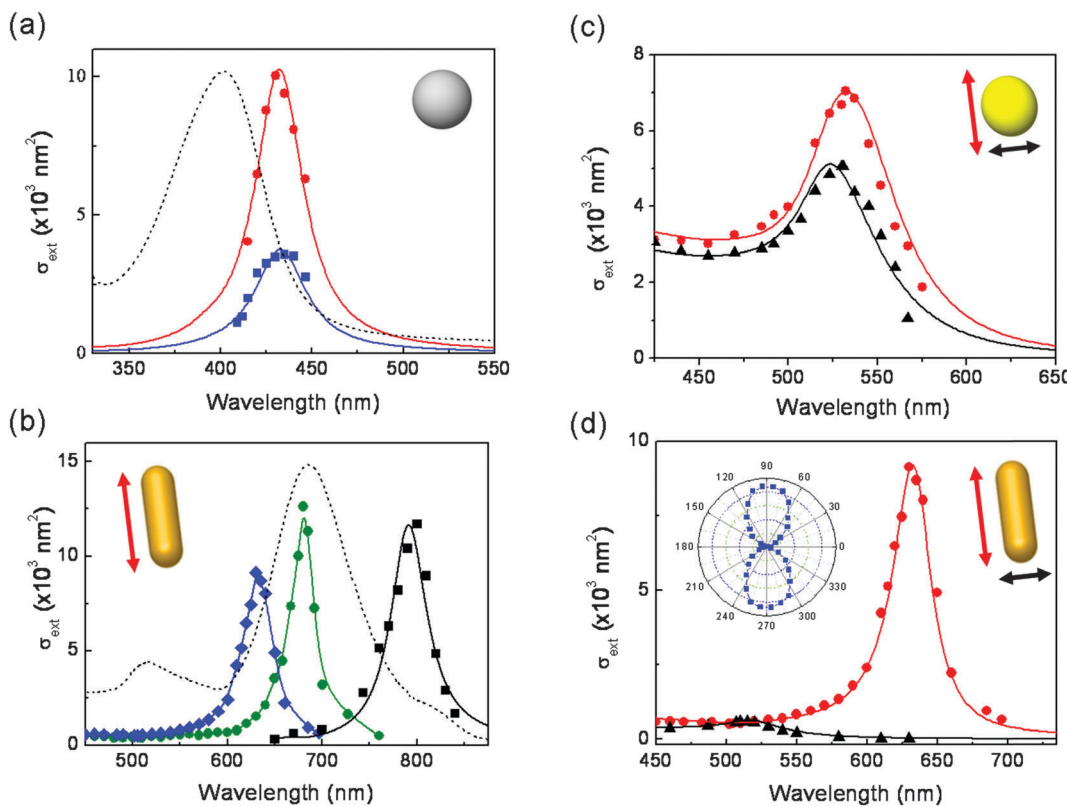


**Fig. 8** Absolute extinction cross-section,  $\sigma_{\text{ext}}$ , spectra of different single metal nanoparticles measured by spatial modulation spectroscopy: (a) silver nanospheres with diameters of 30 nm (circles) and 21 nm (squares). (b) Gold nanorods with aspect ratios of 2.5, 3, and 4 (with increasing SPR wavelength) for light polarized along their main axis (the dotted line shows the absorption spectrum of the initial solution). (c) A quasi-spherical gold nanoparticle for incident light polarized along two perpendicular directions (the wavelength and amplitude changes reflect its slight ellipticity with dimensions of 50 and 46 nm for the long and short axis, respectively). (d) A single gold nanorod for light polarized along its long and short axis (long axis of 20.5 nm and aspect ratio  $\eta = 2$ ). Inset:  $\sigma_{\text{ext}}$  polarization dependence measured at 630 nm. The full lines are fits either by assuming a Lorentzian shape (eqn (15)) in (a) and (b), or the ellipsoidal model (eqn (13)) in (c) or finite element modeling in (d).

This approach was first applied in reflection and with interferometric detection of the probe beam using an additional spatially shifted reference beam (photothermal interference contrast, PIC, Fig. 10a and b).<sup>117</sup> A more sensitive variant, photothermal heterodyne imaging (PHI, Fig. 10c and d) was subsequently developed, permitting detection of the absorption of single gold nanoparticles as small as 1.4 nm<sup>119,120</sup> and of single molecules with less than 1 nm<sup>2</sup> absorption cross-sections in glycerol. Note that the solvent plays a key role in photothermal signal amplitude, and, as expected, larger responses are obtained in liquids with large refractive index dependence on temperature and poor thermal conductivity such as glycerol, pentane and thermotropic liquid crystals.<sup>121,122</sup> The high sensitivity of photothermal techniques being frequently associated to intense illumination, this may limit their application in thermally sensitive media.<sup>121</sup> A simpler detection scheme based on the analysis of the probe beam wavefront on a CCD camera has also been recently developed, but with a reduced sensitivity (nano-objects larger than 100 nm).<sup>123</sup>

As photothermal signals are mostly due to the rise in the temperature of the surrounding media, they strongly depend on heat diffusion kinetics mediated by heat diffusion in the matrix and, for small nanoparticles, the particle–environment

thermal interface resistance.<sup>8</sup> Absorption being indirectly detected, precise connection between the measured signal amplitude and absorption cross-section amplitude is therefore difficult.<sup>124</sup> Though absorption cross-sections have been estimated comparing the magnitude of PHI signals to those obtained from reference nano-objects,<sup>124,125</sup> the axial dependence of the PHI signal can generate systematic errors.<sup>124</sup>

**2.3.2. Other nonlinear optical techniques.** Nonlinear optical detection of single nanoparticles has also been performed using hyper Rayleigh scattering (HRS), also permitting investigation of the mechanisms at its origin. As the measured signal is at a different frequency as compared to the incident beam ( $2\omega$  or  $3\omega$ , for second and third order HRS, respectively,  $\omega$  being the incident laser frequency), it can be spectrally filtered and detected using high sensitivity photon counting methods. Despite the weakness of the signals, single particle detection was thus achieved by third order HRS from individual gold nanoparticles in the 40–150 nm diameter range spin-coated in a polymer solution on glass cover slides.<sup>42</sup> Second order HRS from 150 nm gold nanoparticles dispersed in gelatin was also recently performed,<sup>126</sup> yielding nanoparticle quadratic hyperpolarizabilities in good agreement with those estimated from ensemble studies.<sup>41</sup>

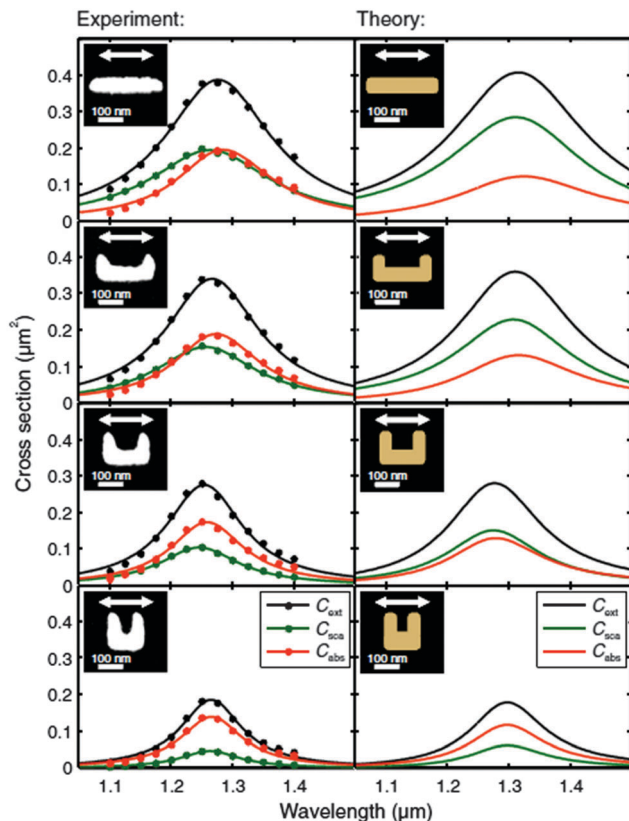


**Fig. 9** Quantitative determination of the absorption, scattering and extinction cross-sections of individual gold nanoantennas combining SMS and interferometric detection. The dots show the measured scattering  $\sigma_{\text{sca}}$ , absorption  $\sigma_{\text{abs}}$ , and extinction cross-section spectra  $\sigma_{\text{ext}}$  (left column, see legend), for incident light horizontally polarized (see double arrow). The insets show electron micrographs of the 35 nm thin gold nanoantennas. The solid lines are Lorentzian fits and the corresponding numerically computed cross-sections are depicted in the right column on the same scale and in the same format for comparison with experimental results. Reprinted with permission from ref. 106 (Copyright 2012 by The American Physical Society).

Nonlinear four-wave mixing techniques have also been used to detect single nano-objects and nanoclusters (whose multiple Fano resonances lead to an enhancement of four-wave mixing signals for a suitable choice of exciting wavelengths<sup>44</sup>). They utilize the same schemes and interaction mechanisms as other ultrafast time-resolved methods based on third order nonlinearities, and can be described in the same context of two-beam interactions as pump-probe methods. By fixing the pump-probe delay and scanning the overlapping pump and probe focal spots over the sample, single-particle imaging can be obtained. These methods will thus be discussed in more detail in Section 5, transient absorption microscopy having been applied to observation of individual metal nanoparticles as well as metallic and semiconductor nanowires<sup>127,128</sup> and carbon nanotubes.<sup>129–131</sup> Four-wave mixing from small gold nanoparticles (down to the 5 nm range) has also been demonstrated to be applicable to cell imaging, taking advantage of signal enhancement using incident light in resonance with their surface plasmon resonance and background free signal detection.<sup>132</sup>

#### 2.4. Morphological characterization and optical study of a nano-object

Determination of the optical properties of a single nano-object provides crucial physical information provided additional input can be obtained on its morphology and composition. The optical response strongly depending on the object size and shape, their determination is necessary for accurate interpretation and modeling of the experimental results. This has fostered the development of experimental methods for combining optical measurements on a single nano-object and morphological characterization using high spatial resolution imaging tools. This correlation has been mostly done for nano-objects deposited on a substrate using atomic force microscopy (AFM)<sup>65,89,97,133</sup> or electron microscopy. The former approach is however limited by a slow imaging rate over the usually large area used in far-field optical imaging (extending over tens of micrometers, individual nano-objects being separated by more than 1 μm to permit their optical distinction).<sup>65</sup> In the latter case, transmission electron microscopy (TEM) is most widely used but requires specific substrates compatible with both optical and electronic imaging (e.g., a few tens of nanometer thick silica, silicon nitride, formvar or carbon layer deposited on a TEM grid).<sup>82,134–136</sup> Scanning electron microscopy (SEM) has also been used, but requires conducting substrates such as ITO to reach a sufficient spatial resolution.<sup>79,133</sup> Combining quantitative single-particle optical techniques as SMS with electron microscopy studies has opened unprecedented possibilities of comparing experimental spectra with theoretical models (e.g., standard and generalized Mie theories for spheroids and wires in simple enough environments,<sup>25,137</sup> or for more complex situations numerical approaches such as discrete-dipole approximation,<sup>138</sup> boundary element method,<sup>139</sup> finite difference time domain<sup>44,140</sup> and finite element modeling<sup>141</sup>), using nano-object morphology as an input.<sup>135</sup>

Nanoparticle and substrate exposure to a high electron flux has however been demonstrated to alter the measured optical spectra, therefore precise particle characterization has to be performed after the optical measurements.<sup>108,136</sup> Crude initial selection and identification of an object to be optically investigated can however be performed using low magnification imaging. Such initial TEM identification is a useful approach when the nano-objects of interest are in minority in the sample.<sup>46,108</sup> While most commonly used in its standard form yielding two-dimensional images, electron microscopy correlation can also be performed using three-dimensional tomography,<sup>142</sup> a particularly important input when complex morphology nano-objects are studied, such as core-shell nanoparticles.<sup>143</sup>

### 3. Linear optical response of metal nano-objects

Because of the very efficient non-radiative intraband electronic state relaxation enabled by electron-lattice coupling in metallic materials, their luminescence quantum yield after photoexcitation is very low.<sup>144</sup> In the case of metallic nano-objects,

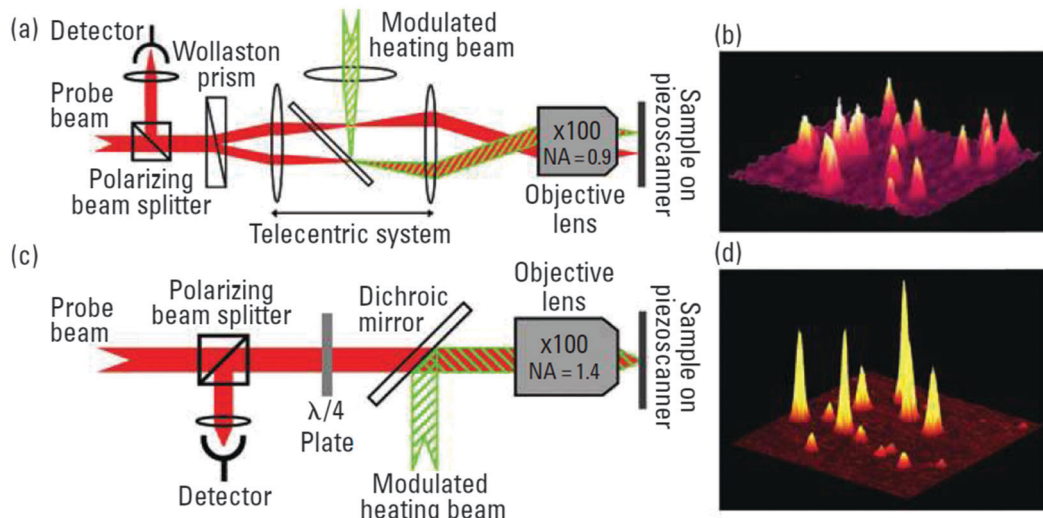


**Fig. 10** Schematic setup for photothermal imaging of individual nano-objects: (a) photothermal interference contrast (PIC) and (c) photothermal heterodyne imaging (PHI). PIC and PHI images of a  $10 \times 10 \mu\text{m}$  region show individual 5 nm diameter gold nanoparticles (b) and a mixture of individual 2 nm (small peaks) and 5 nm diameter (large peaks) gold nanoparticles (d). Reprinted with permission from ref. 299 (Copyright 2008 American Chemical Society).

photoluminescence has been observed for few-atom clusters, which exhibit molecular-like behaviors, and some small silver particles.<sup>145,146</sup> Plasmonic effects have enabled detection of luminescence due to interband recombination of individual nano-objects as gold nanorods and nanospheres,<sup>38,39,147</sup> with promising applications in biological imaging, that will not be discussed here.

The non-luminescent methods described above have been extensively used to investigate the fundamental properties of metallic nano-systems. In particular, much information has been obtained on their linear optical response and on the spectral characteristics of their SPRs as a function of the nano-object morphology and environment. They are illustrated below for isolated metallic objects and interacting ones (dimers).

### 3.1. Isolated metal nano-objects

#### 3.1.1. Surface plasmon resonances of metal nano-objects.

Reduction of the size of a metal particle to the nanoscale leads to appearance of novel optical resonances in its linear and nonlinear optical response.<sup>13,14,19,48,148</sup> This phenomenon was described theoretically by Mie in the case of spherical inclusions of arbitrary size dispersed in a homogeneous dielectric medium.<sup>25</sup> For small particle sizes compared with the optical wavelength (smaller than typically  $\lambda/10$ ), it can be classically associated to homogeneous oscillation of the metal electrons with the electromagnetic field, and simply described in the dipolar approximation of the Mie theory, *i.e.*, assimilating the nanoparticle scattered field to that of a dipole (Fig. 11a). This dipolar response exhibits resonances, the dipolar localized SPRs, corresponding to resonances between the electronic movement and electromagnetic field frequency, and associated to large field enhancements in and around the particle (local field effect).<sup>14,148</sup> Equivalent results are obtained using the quasistatic approximation consisting in assuming that the incident electromagnetic

field is uniform over the particle (*i.e.*, neglecting retardation effects). Conversely, additional multipolar SPRs are observed for larger particles, as the incident electromagnetic field cannot be considered to be uniform over the particle (Fig. 11a).<sup>25</sup>

The spectral features of nanoparticle SPRs in their scattering and absorption spectra (peak wavelength, lineshape, polarization, amplitude) depend on its composition, morphology and

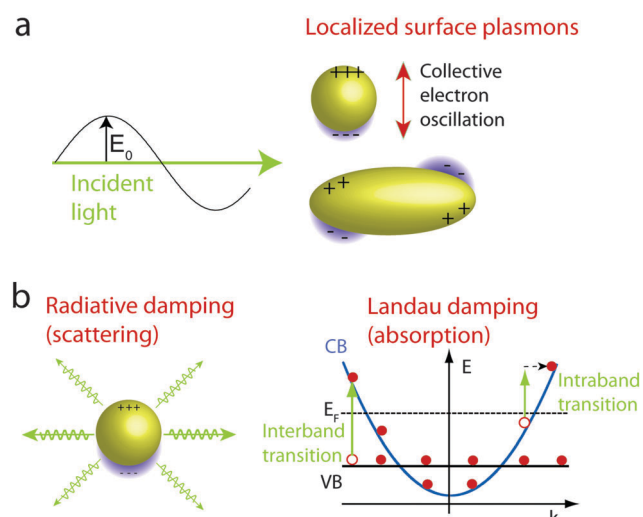


**Fig. 11** (a) Schematic electron displacement associated to the localized surface plasmon resonance of a metal nanoparticle: a collective displacement is induced by an incident light beam for an object much smaller than the light wavelength, resulting in a dipolar response, while a non-uniform displacement occurs for nano-objects with a larger size along the propagation direction of the incident light wave, exciting higher-order plasmon modes. (b) Plasmon decay mechanisms via radiative (elastic scattering of the incident light) and non-radiative (Landau damping, *i.e.*, single electron–hole excitations) processes. The latter can take place by intraband (a conduction band, CB, electron is excited to an unoccupied CB state) or interband (excitation of a valence band VB electron in the CB) transitions.

environment.<sup>148,149</sup> This is clearly illustrated for an ellipsoidal particle in a homogeneous matrix, for which the scattering and absorption (or extinction) cross-sections can be analytically computed in the quasistatic regime (with  $\sigma_{\text{scat}}/\sigma_{\text{abs}} \propto V/\lambda^3 \ll 1$  in this regime):<sup>58</sup>

$$\begin{aligned}\sigma_{\text{scat}}^i &= \frac{\omega^4 V^2 \epsilon_m^2}{6\pi c^4 L_i^2} \frac{[\epsilon_1(\omega) - \epsilon_m]^2 + \epsilon_2^2(\omega)}{\left[ \epsilon_1(\omega) + \frac{1-L_i}{L_i} \epsilon_m \right]^2 + \epsilon_2^2(\omega)} \\ \sigma_{\text{ext}}^i \approx \sigma_{\text{abs}}^i &= \frac{\omega V \epsilon_m^{3/2}}{c L_i^2} \frac{\epsilon_2(\omega)}{\left[ \epsilon_1(\omega) + \frac{1-L_i}{L_i} \epsilon_m \right]^2 + \epsilon_2^2(\omega)}\end{aligned}\quad (13)$$

where  $\omega$  is the incident light frequency,  $V$  the nanoparticle volume,  $\epsilon$  its dielectric function and  $\epsilon_m$  the dielectric function of the matrix (assumed real and undispersed).  $L_i$  are shape-dependent factors characterizing the response for light polarized along the  $i$  axis of the ellipsoid.<sup>58,60</sup> For instance, all  $L_i$  equal 1/3 for nanospheres, while for a prolate spheroid of eccentricity  $e = \sqrt{1 - a^2/c^2}$  (with  $a$  and  $c$  the lengths of its minor and major axes) the  $L_i$  are given by  $L_c = (1/e^2 - 1)(\ln[(1+e)/(1-e)]/(2e) - 1)$  and  $L_a = (1 - L_c)/2$  for major and minor axis directions, respectively.

The dipolar SPR corresponds to maxima of  $\sigma_{\text{scat}}$  and  $\sigma_{\text{abs}}$ , *i.e.*, as a first approximation to minima of their denominator. For a noble metal, the complex dielectric function  $\epsilon = \epsilon_1 + i\epsilon_2$  can be separated into contributions associated to intraband (Drude-like) and interband ( $\epsilon^{\text{ib}} = 1 + \chi^{\text{ib}}$ ) transitions<sup>14,150</sup> (Fig. 11b):

$$\epsilon(\omega) = \epsilon^{\text{ib}} - \frac{\omega_p^2}{\omega(\omega + i\gamma)} \approx \epsilon^{\text{ib}} - \frac{\omega_p^2}{\omega^2} + i \frac{\omega_p^2 \gamma}{\omega^3} \quad (14)$$

where  $\omega_p$  is the plasma frequency of the metal and  $\gamma$  the optical scattering rate of the conduction electrons in the nanoparticle (with  $\gamma \ll \omega$  in the visible range). It is modified by reduction of the nanoparticle size below the electron mean free path in the bulk metal (typically in the 20–50 nm range). The effect of electron confinement in the particle has thus to be introduced, yielding a scattering rate  $\gamma$  that can be written as the sum of a bulk-like rate  $\gamma_0$  and a quantum confinement term:  $\gamma = \gamma_0 + \gamma_s$ .<sup>14</sup> Note that quantum effects significantly alter  $\epsilon$  only *via* the scattering rate  $\gamma$  for sizes down to about 2–3 nm.<sup>150,151</sup>

If  $\epsilon^{\text{ib}}$  is small or weakly dispersed close to the SPR frequency (*i.e.*, if the SPR frequency is below the interband transition threshold in noble metals, *e.g.* for silver nanospheres or elongated gold nano-objects),  $\sigma_{\text{abs}}$  spectrum (eqn (13)) displays a quasi-Lorentzian profile characterized by only three independent parameters, namely spectral position ( $\Omega_R$ ), integrated area ( $\Xi$ ) and width ( $\Gamma$ ):

$$\sigma_{\text{abs}}(\omega) = \Xi \frac{\Gamma/(2\pi)}{(\omega - \Omega_R)^2 + (\Gamma/2)^2} \quad (15)$$

For both scattering and absorption, the frequency  $\Omega_R$  of the dipolar SPR is then simply given by the condition  $L_i \epsilon_1(\Omega_R) + (1 - L_i) \epsilon_m = 0$ , depending on the nanoparticle composition (*via*  $\epsilon_1$ ), morphology (*via*  $L_i$ ) and environment (*via*  $\epsilon_m$ ).<sup>14</sup>

The integrated areas are given by  $\Xi_{\text{abs}} = \pi V \epsilon_m^{3/2} \Omega_R^4 / (2c L_i^2 \omega_p^2)$  and  $\Xi_{\text{scat}} = V^2 \epsilon_m^4 \Omega_R^{10} / (12 \gamma c^4 L_i^4 \omega_p^4)$  and the linewidth  $\Gamma$  by:<sup>60,152</sup>

$$\begin{aligned}\Gamma &= \Gamma_{\text{nr}} = \left[ \gamma + \frac{\epsilon_2^{\text{ib}}(\Omega_R) \Omega_R^3}{\omega_p^2} \right] \Bigg/ \left[ 1 + \frac{\Omega_R^3 \partial \epsilon_1^{\text{ib}}}{2\omega_p^2 \partial \omega} \Big|_{\Omega_R} \right] \\ &\approx \gamma + \frac{\epsilon_2^{\text{ib}}(\Omega_R) \Omega_R^3}{\omega_p^2} = \gamma + \Gamma_{\text{ib}}\end{aligned}\quad (16)$$

This expression includes only the non-radiative contribution  $\Gamma_{\text{nr}}$ , as SPR radiative damping is concomitant with retardation effects and is thus neglected in the dipolar approximation considered here.  $\Gamma_{\text{nr}}$  is a consequence of Landau damping of the collective electron-electromagnetic oscillation into intraband (first term in eqn (16)) or interband (second term in eqn (16)) single electron-hole pair excitation, *i.e.*, damping of the collective mode by intraband or interband absorption (Fig. 11b). The interband term is important when the SPR overlaps the interband transition threshold and can thus be damped *via* excitation of d-electrons to the conduction band state above the Fermi energy. The created d-holes then relax on few tens of femtosecond timescale by Auger relaxation, leading to electron-hole pairs in the conduction band.<sup>153,154</sup> Intraband damping takes place in all systems and dominates when the SPR is away from the interband transitions. It is a consequence of the electron scattering, *i.e.*, electron-electron, electron-ion and electron-defects ( $\gamma_0$  term), leading to damping of the coherent electronic motion associated to the SPR by excitation of electron-hole pairs in the conduction band.<sup>14,60,153,155</sup> For small particles, electron-surface scattering also contributes, modifying the global scattering rate ( $\gamma_s$  term).<sup>14,156,157</sup> In both cases, *i.e.*, interband and intraband SPR relaxation, the excited electron-hole pairs relax by electron-electron scattering in the conduction band, leading to a hot electron distribution on a size-dependent timescale of few hundred femtoseconds.<sup>158,159</sup> This cools down by energy transfer to the lattice, *i.e.*, electron-phonon scattering in a bulk-like system, eventually leading to a fully thermalized particle.<sup>3,160</sup> Electron-hole pairs can also lose their energy by external coupling to the surrounding environment, depending on its nature.<sup>161</sup>

For larger nano-objects, retardation effects and radiative damping (Fig. 11b) lead to a red-shift and broadening of the dipolar SPR, concomitant with appearance of additional resonances.<sup>25,148</sup> Radiative damping ( $\Gamma_r$ ) reflects relaxation of the collective oscillation by emission of light, and is thus associated to nanoparticle light scattering, increasing with the particle volume in the small size regime.<sup>162,163</sup> Radiative and non-radiative contributions can be added so that the total damping rate  $\Gamma$  is given by:

$$\Gamma(\Omega_R) = \Gamma_r(\Omega_R) + \Gamma_{\text{nr}}(\Omega_R) = \Gamma_r(\Omega_R) + \Gamma_{\text{ib}}(\Omega_R) + \gamma_0 + \gamma_s \quad (17)$$

This expression contains intrinsic mechanisms to the SPR width for a nanoparticle embedded in a dielectric,  $\gamma_s$  also lumping possible additional contributions due to chemically bound molecules (chemical damping).<sup>150,152,164</sup>

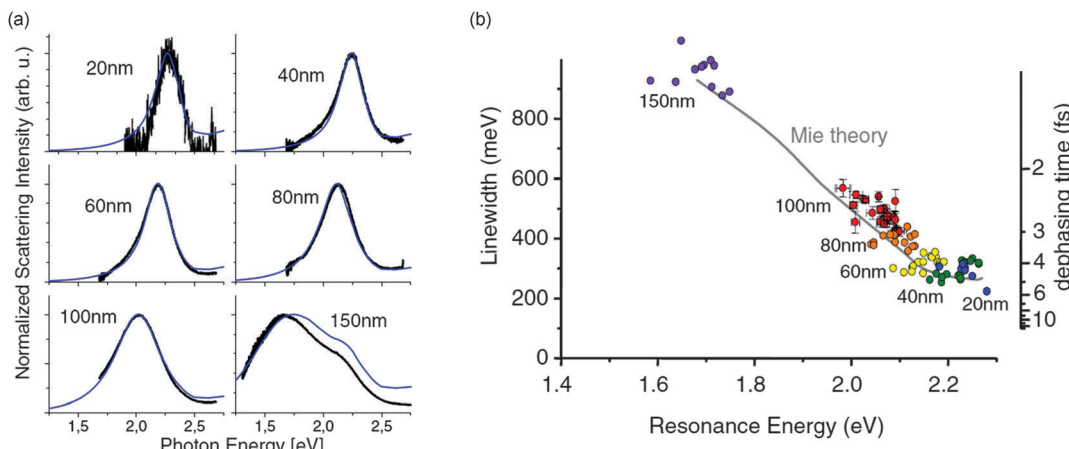


**Fig. 12** (a) Scattering spectra of single gold nanospheres with different diameters. The blue curves show the results of Mie theory calculations using the dielectric function of gold.<sup>184</sup> (b) Measured linewidth of the SPR of single gold nanospheres as a function of the SPR energy (symbols) for different nanoparticle mean diameters as indicated. The full line shows the result of Mie theory. Adapted with permission from ref. 92 (Copyright IOP Publishing & Deutsche Physikalische Gesellschaft. CC BY-NC-SA).

**3.1.2. Single metal nanoparticle absorption and scattering spectra.** The scattering and extinction spectra of single metal nano-objects with different shapes have been studied using the above-described methods, including spheres,<sup>92,109,110,165,166</sup> rods,<sup>78,79,112,157,167</sup> prisms,<sup>57,133</sup> shells,<sup>168,169</sup> disks,<sup>102,170</sup> cubes,<sup>171,172</sup> and bipyramids<sup>108</sup> (investigation of the optical properties of 2D confined nanowires has also been performed,<sup>173,174</sup> but will not be discussed in this review). As expected, the scattering, extinction or absorption spectra of nano-objects with sizes below about 100 nm are dominated by their dipolar SPRs. They exhibit Lorentzian lineshapes (eqn (15)) when the SPR lies below the interband transition threshold, *e.g.* for silver and elongated gold nano-objects (Fig. 5b, 8a and b).<sup>78,108,133,156,157</sup> Conversely, when the SPR overlaps with the interband transitions (as encountered for gold or copper nanospheres), asymmetric extinction spectra are obtained (Fig. 8c) while the scattering ones maintain quasi-Lorentzian shapes (Fig. 12).<sup>92,105,165</sup> This is a consequence of the dispersion of the interband part of  $\varepsilon_2$  that significantly alters  $\sigma_{\text{abs}}$  but more weakly  $\sigma_{\text{scat}}$  (different numerator for  $\sigma_{\text{abs}}$  and  $\sigma_{\text{scat}}$  in eqn (13), reflecting the different processes enhanced by the SPR effect). Red shift and broadening are experimentally observed for increasing size. For larger sizes (above about 100 nm), the SPR lineshape significantly deviates from a simple Lorentzian due to multipolar effects, in excellent agreement with theoretical models (Fig. 12a).<sup>14</sup>

**3.1.3. Substrate effects.** Most single-particle investigations are performed on nano-objects deposited on a dielectric substrate. Though the results are frequently interpreted in the approximation of the homogeneous environment with an effective mean dielectric constant<sup>175,176</sup> (for instance using eqn (13) for small nanoellipsoids), more precise modeling requires to take into account the asymmetry of the object environment (unless the object is encapsulated). In the case of a metal nano-object, the primary signature of the presence of a substrate with higher refractive index  $n_s$  than the surrounding medium  $n_m$  (Fig. 13a) is a red shift (as compared to a uniform  $n_m$  medium) of the dipolar SPRs as seen, *e.g.*, in

the scattering spectra of gold nanorods on ITO<sup>177</sup> and silver nanocubes on glass.<sup>172</sup> A reduced sensitivity on  $n_m$  changes (as compared to the homogeneous environment) is also observed, as demonstrated in dark-field studies of gold nanoprisms.<sup>175</sup> These effects can be phenomenologically accounted for by defining a mean homogeneous environment of the nano-objects, characterized by a mean refractive index  $n_{\text{eff}} = \alpha n_m + (1 - \alpha)n_{\text{sub}}$ , where  $\alpha$  is used as a parameter ( $\alpha \approx 0.5$  for prisms deposited on glass<sup>175</sup>). This approach also permits a good reproduction of both the extinction spectra and amplitudes measured by SMS,<sup>108,112</sup> but can only be considered as a crude approximation as it neglects the actual asymmetry of the environment.

This clearly shows up in the induced asymmetrical optical response of symmetrical objects along directions in and perpendicular to the substrate plane. It leads to a light polarization dependence of the measured spectra increasing with the ratio  $n_s/n_m$ , as observed in dark-field measurements of deposited gold nanoshells and nanospheres using obliquely incident light.<sup>169</sup> This effect can be accounted for by modeling the effect of the substrate using the concept of image charge.<sup>178</sup> For a small nano-object-substrate distance, the large nonuniformity of the electromagnetic fields created in a nanoparticle by its image leads to excitation of quadrupolar and higher order modes, which are otherwise not activated for small nano-objects in a uniform environment. This substrate-induced hybridization between different SPR modes leads to a transition from a dipolar SPR response to a multipolar SPR as the object-substrate distance is reduced.<sup>137,179,180</sup> For instance, the double structure observed in the scattering spectra of single 30 nm silver nanocubes on glass<sup>172,181</sup> was ascribed to hybridization between dipolar and quadrupolar modes.<sup>182</sup> Hybridization effects were also observed for gold nanorods deposited on silicon but disappeared for deposition on glass (due to reduction of substrate refractive index) or increase of the nanorod-silicon distance using a spacer layer.<sup>183</sup>

Substrate effects can be strongly reduced by encapsulating the metal nano-objects in a dielectric shell.<sup>135,156</sup> This is a

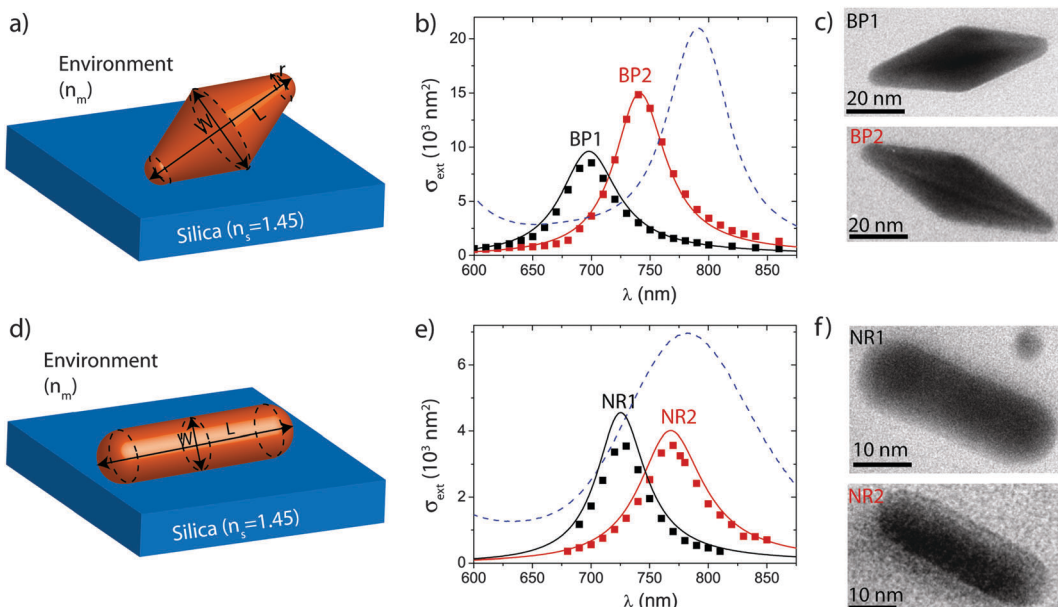


**Fig. 13** Extinction cross-section spectra and amplitude measured by SMS for individual nano-bipyramids (b) and nanorods (e) deposited on a glass substrate, with model shapes shown in (a) and (d), and TEM measured morphology in (c) and (f). The full lines in (b) and (e) are fits of the individual extinction spectra using the TEM measured sizes of the nano-objects and the environment refractive index  $n_m$  as a parameter. The theoretical width has been adjusted to the experimental one. The dashed lines in (b) and (e) are the normalized ensemble extinction spectra of the initial colloidal solutions. Reprinted with permission from ref. 108 (Copyright 2012 American Chemical Society).

consequence of the fact that the optical response around the SPR wavelength of a metal nanoparticle is mostly sensitive to its close environment, at a distance over which the local field is enhanced (*i.e.*, of the order of radius for a nanosphere and width for a nanorod).<sup>14,105</sup> For a shell thickness of comparable or larger size, the shell provides a quasi-homogeneous environment to the metallic core, masking the outside environment, a particularly interesting situation for quantitative comparison of experimental and theoretical results.

**3.1.4. Input of quantitative spectroscopies.** Comparison of the measured and computed spectral response of a single nano-object is particularly relevant when its morphology is independently determined. This has been mostly done by combining TEM or SEM imaging with the SMS technique, as it provides the amplitude of the measured cross-sections (Fig. 9 and 13).<sup>46,106,108,134,135</sup> The only unknown parameter in experiment/theory comparison is then the object local environment, which can however be fixed during its synthesis, for instance by its encapsulation in a shell of known optical properties. For a sufficient shell thickness, the SPR properties are weakly sensitive to the external environment, which can be considered as homogeneous and set by the shell dielectric constant.<sup>135,156</sup> Using numerical simulations with the measured particle size, shape and orientation, excellent reproduction of the experimental polarization-dependent spectra was thus obtained without free parameters. This is illustrated in Fig. 14 for silica-encapsulated gold nanorods deposited on a substrate. All the parameters describing the SPR, *i.e.*, its frequency, linewidth and integrated area (eqn (15)) are perfectly reproduced (the dielectric function of bulk gold<sup>184</sup> has been used, confinement effects playing a minor role for the

large nanorods investigated). Note that the accuracy of the tabulated bulk metal dielectric functions<sup>185</sup> is now one of the limiting aspects, especially in the case of silver.<sup>109,156,167</sup>

Comparison is more difficult for non-encapsulated nano-objects, due to the necessity of correctly describing their (partly unknown) local surroundings. Experiments performed on deposited non-encapsulated gold nanorods and nanobipyramids show that taking into account the substrate in the simulation (assuming the above medium is air, Fig. 13a and 14a) is insufficient to properly describe the SPR frequency of the measured  $\sigma_{ext}$  spectra<sup>108,135</sup> (Fig. 14b). Excellent agreement can be obtained by adjusting the refractive index  $n_m$  of the medium embedding the object above the substrate (Fig. 13 and 14).<sup>108</sup> The experimentally determined values suggest the presence of surfactant molecules, residual solvent, or water around the deposited particles, in agreement with recent theoretical modeling assuming a water droplet around the nano-objects.<sup>135</sup> This hypothesis is also supported by large variations of the effective  $n_m$  value for nanoparticles originating from the same or differently synthesized colloidal solutions.<sup>105,108</sup>

The ability of classical electromagnetism simulations to reproduce the position and area of single-particle optical spectra enables the use of the optical response of a nano-object to extract information on its morphology and orientation, provided it exhibits a simple shape. For instance, for small quasi-spherical objects (with a diameter  $< 20 \text{ nm}$ ),  $\Omega_R$  is mainly determined by the particle environment (eqn (13)),<sup>16,110</sup> while  $\Xi$  depends on both the particle volume and the environment refractive index. Fitting of the measured  $\sigma_{ext}$  spectrum and amplitude permits determination of both parameters, as well as its shape anisotropy from the

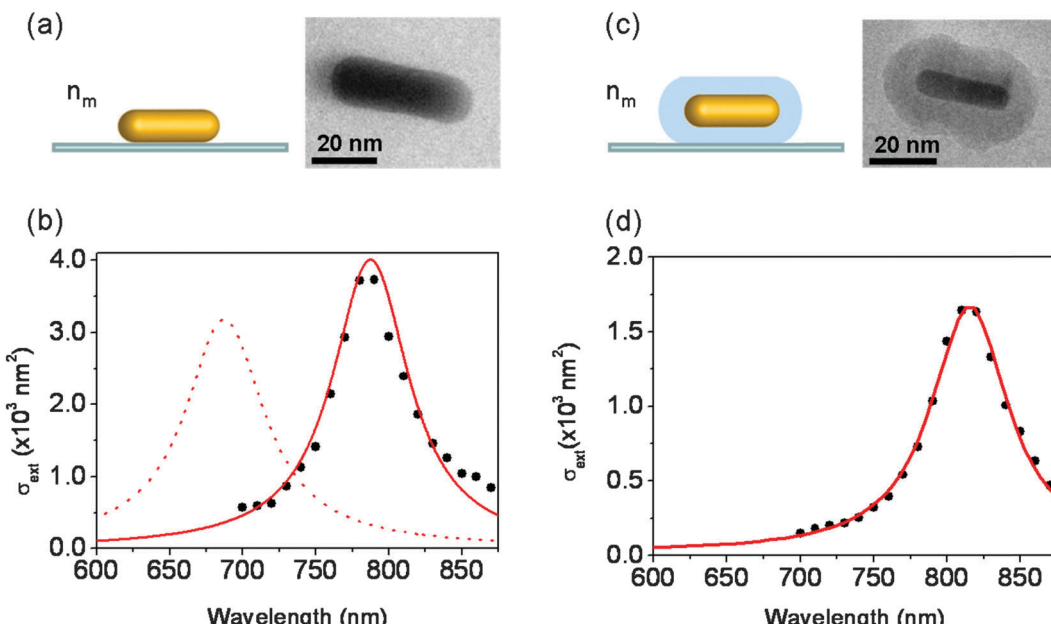


Fig. 14 Simulated (solid and dotted lines) and measured (dots) absolute extinction cross-sections of (b) bare and (d) silica-coated gold nanorods, deposited on a 40 nm thick silica substrate in air, as schematically shown in (a) and (c) respectively, together with their TEM images. The results of numerical simulation of the extinction spectra performed by FEM using the TEM measured sizes of the nanoparticles (in (a) and (c)) and including the silica substrate are shown for  $n_m = 1$  (dotted line) and  $n_m = 1.3$  (full line) in (b), and for  $n_m = 1$  for the coated nanorod (d), stressing the importance of particle environment control.

polarization-dependent  $\sigma_{\text{ext}}$  spectra ( $L_i$  factors in eqn (13)).<sup>105,134,156</sup> For more complex morphologies, such as nanorods and nanobipyramids, the dependencies of  $\sigma_{\text{ext}}$  on the characteristics of the particle and its environment cannot be easily disentangled, and its dimensions can be optically determined only if its environment is known (e.g., if it is embedded or encapsulated in a dielectric medium of known refractive index, as discussed above).<sup>108,112,135,157</sup>

**3.1.5. Surface plasmon resonance width.** The spectroscopy of a single nano-object offers the important possibility to measure the homogeneous width  $\Gamma$  of its SPRs, a parameter most usually masked by inhomogeneous broadening effects due to morphology dispersion in ensemble measurements. As introduced above (Section 3.1.1), provided it can be properly defined (*i.e.*, for sufficiently weak  $\varepsilon^{\text{ib}}$  dispersion),  $\Gamma$  is set by the bulk-like electron scattering rate  $\Gamma_{\text{ib}} + \gamma_0$ , the confinement effect contribution  $\gamma_s$  (for small sizes) and the radiative contribution  $\Gamma_r$  (for large sizes) (eqn (17)). Experimental measurement of  $\Gamma$  is thus of particular interest for determining the impact of quantum confinement, as its dependencies on the particle size and shape are still largely unknown.

The contribution  $\gamma_s$  rises with reducing particle size, as quantum confinement effects become more important. In the case of a nanosphere,  $\gamma_s$  has been predicted by both classical and quantum theories<sup>14,152,162,186,187</sup> to be inversely proportional to its diameter  $D$ :

$$\gamma_s = 2g_s \frac{v_F}{D} \quad (18)$$

where  $v_F$  is the metal Fermi velocity and  $g_s$  a parameter of the order of unity. SMS experimental measurements of the SPR spectra of quasi-spherical silver nanoparticles ( $\text{Ag}@\text{SiO}_2$ , encapsulated in

silica to protect them from oxidation and prevent any spurious interface damping mechanism) have shown the expected rise of  $\gamma_s$  with  $1/D$  (Fig. 15).<sup>156</sup> This behavior is observed in the small size regime where  $\Gamma_r$  is negligible, for  $D$  smaller than 25 nm, yielding an effective  $g_s = 0.7 \pm 0.1$  (which lumps all surface-induced changes of  $\gamma$ , including those of  $\gamma_0$ ).<sup>156</sup> Subtraction of the estimated size-dependence of  $\gamma_0$  yields the corrected value  $g_s = 0.45 \pm 0.1$ . This value is smaller than that predicted by Kawabata and Kubo assuming infinite confinement potential of the electrons,<sup>162</sup> but consistent with recent numerical calculations based on a time-dependent local density approximation using a more realistic confinement potential.<sup>152,188</sup> A smaller  $g_s$  value was reported by investigating the absorption spectra of single gold nanospheres by photothermal spectroscopy.<sup>165</sup> However, the uncertainties associated to the non-Lorentzian SPR profile of gold nanospheres (Fig. 8c) and the absence of individual size determination make the extracted values compatible with the previous ones.<sup>156</sup>

A similar SMS approach was recently used to investigate the width of longitudinal SPR in gold nanorods ( $\text{Au}@\text{SiO}_2$  nanorods whose length  $L$  and diameter  $D$  were determined either by optics or by TEM correlation).<sup>157</sup> As  $\gamma_0$  and  $\Gamma_r$  (eqn (17)) are almost constant for the studied sizes, the measured dependence of  $\Gamma$  on both  $L$  and  $D$  mostly reflects that of  $\gamma_s$  (Fig. 16). A dependence proportional to  $S^{-1/2}$ , introducing the rod surface  $S = \pi LD$ , is found *i.e.*  $\gamma_s \approx Av_F/(L^{1/2}D^{1/2})$  with  $A = 1.4$  (Fig. 16c and 17).<sup>157</sup> This dependence is fully consistent with that measured in silver spheres (eqn (18)),<sup>156</sup> replacing  $D$  by an effective length  $L_{\text{eff}} = (S/\pi)^{1/2}$ . Measurements of the SPR width of gold nanorods deduced from  $\sigma_{\text{scat}}$  measurements using dark-field spectroscopy

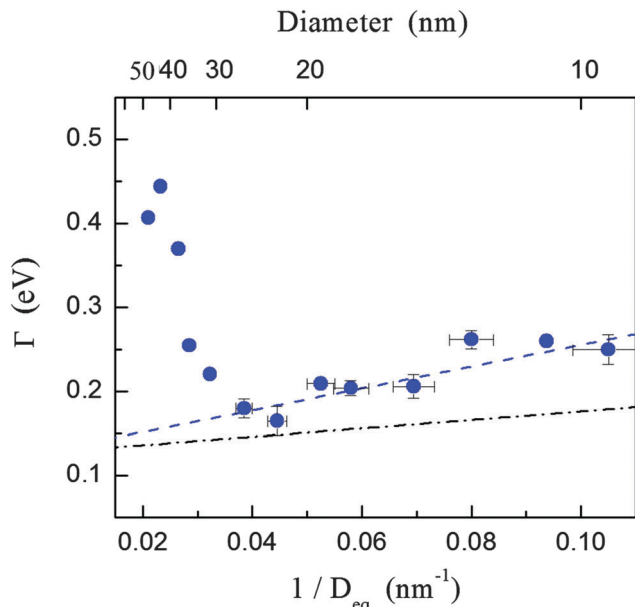


Fig. 15 Spectral width  $\Gamma$  of the SPR measured in different single Ag@SiO<sub>2</sub> nanoparticles as a function of the inverse of their equivalent diameter  $D_{\text{eq}}$ , optically determined by fitting the  $\sigma_{\text{ext}}$  spectra. Error bars on size determination and width are indicated for three typical sizes. The blue dashed line is a linear fit using eqn (18) with  $g_s = 0.7$  and  $\gamma_0 = 0.125 \text{ eV}$ . The dash-dotted line is the estimated size variation of the intrinsic electron scattering rate. Adapted with permission from ref. 156 (Copyright 2009 American Chemical Society).

show consistent results, when mean values are used for their sizes (as these were not individually determined but only from statistics on the initial colloidal solution)<sup>78,79,167</sup> (Fig. 17). These experimental results however strongly differ from the predictions of existing simple quantum models<sup>189</sup> ( $\gamma_s \propto 1/L$ ) and classical billiard approaches ( $\gamma_s \propto 1/D$  for elongated nano-objects<sup>190</sup>), stressing the importance of developing more detailed theoretical models. The SPR width of other shape single nano-objects was also measured using dark-field spectroscopy: oblate gold nanoprisms<sup>133,191</sup> and gold nanoshells.<sup>168,192</sup> While the SPR width could be interpreted using the same expression as for gold nanorods<sup>157</sup> in the former case, the large contribution of radiative damping precluded a quantitative extraction of surface effects in the latter case.

The SPR width has been experimentally shown to strongly depend on the interface between the nanoparticles and their environment (e.g., nature of the matrix, or number and nature of bound molecules), an effect even observable in ensemble studies.<sup>150</sup> In the context of single particle investigation, large SPR broadening and large particle to particle variations have been observed for surfactant-stabilized nanoparticles,<sup>105,108,193</sup> as compared to silica-encapsulated nano-objects.<sup>156,157</sup> The impact of ligands was clearly stressed by investigating the linewidth of gold nanorods for distinct coating procedures.<sup>194</sup> Comparison of measurements for no, tip-specific, and full functionalizations of the same nanorods suggests a linear relation between the SPR broadening and surfactant density, with surface broadening effects, i.e.,  $\gamma_s$  values, also much larger

than the ones measured in silica-coated rods. The SPR width has also been demonstrated to depend on the nature of the bound molecules, determining the SPR homogeneous width using hole burning experiments on ensembles of silver nanospheres.<sup>164</sup> Though precise modeling of chemical damping still has to be developed, the influence of the density and nature of bound molecules is consistent with the sensitivity of the computed SPR width on the details of the electron confinement potential.<sup>152,188</sup>

The impact of quantum effects is expected to become even larger for very small nanoparticles (smaller than 5 nm), a regime not yet investigated at the single-particle level using optical techniques. However, large dipolar SPR broadening has been recently demonstrated using electron energy loss spectroscopy (EELS) on single ligand-free silver nanoparticles in the 2–10 nm size range.<sup>195</sup> The broadening amplitude is larger than expected from optical investigations and associated to a large SPR red shift, in contrast to the small blue shifts computed and observed in optical ensemble studies,<sup>152,196</sup> raising the question of the influence of the carbon substrate and/or of the atomistic surface structure on the measured properties.<sup>196</sup>

For a given morphology, the SPR of large nanoparticles (size above about 30–40 nm) broadens with an increase in their size due to fast increase of the radiative damping contribution (eqn (17)). This effect has been experimentally demonstrated with ensemble measurements<sup>197</sup> and confirmed by single-particle dark-field (Fig. 12) and SMS studies (Fig. 15).<sup>47,78,79,92,133,156,198</sup> In agreement with theoretical predictions using simple analytical models,<sup>14,162,163</sup> linear variations of  $\Gamma_r$  with the particle volume  $V$  ( $\Gamma_r = \kappa V$ ) were experimentally observed for gold nanospheres<sup>92</sup> (Fig. 12), nanorods<sup>78,198</sup> and silver nanoprisms.<sup>133</sup> The  $\kappa$  value has been found to largely depend on the particle composition and shape, as predicted by analytical calculations,<sup>163</sup> with  $\kappa \approx 5 \times 10^{-7} \text{ eV nm}^{-3}$ ,  $8 \times 10^{-7} \text{ eV nm}^{-3}$  and  $1.6 \times 10^{-6} \text{ eV nm}^{-3}$  for gold nanospheres, nanorods (with aspect ratios between 2 and 4), and  $\approx 12 \text{ nm}$  thick oblate silver nanoprisms, respectively.<sup>47,78,133,198</sup>

Radiative damping  $\Gamma_r$  dominates the SPR width for very large nano-objects (with dimensions larger than 100 nm). For these sizes, analysis of scattering spectra of complex-shaped single gold nano-objects (cubes, triangles, octahedra, decahedra and icosahedra) demonstrated a linear dependence of  $\Omega_R$  and  $\Gamma_r$  on a “plasmon length” (defined as the distance between regions of opposite charge associated to dipolar mode electron oscillations)<sup>82</sup> (Fig. 18). Additionally, in this regime,  $\sigma_{\text{ext}}$  and  $\sigma_{\text{scat}}$  spectra display complex, non-Lorentzian shapes as they lump the contribution of various multipolar, spectrally overlapping plasmon modes<sup>82,199</sup> (Fig. 18).

### 3.2. Interacting nano-objects

Interaction of two or more nanoparticles separated by a nanometric distance offers many new and largely unexplored possibilities for designing novel nano-objects and nanomaterials. In particular, multi-component nano-objects formed by different nanoparticles offer the possibilities to combine their different physical or chemical properties (optical, electrical, magnetic, catalytic, etc.) or to create new ones via their interaction.<sup>6,180,200</sup> This field is rapidly growing in the context of the optics of

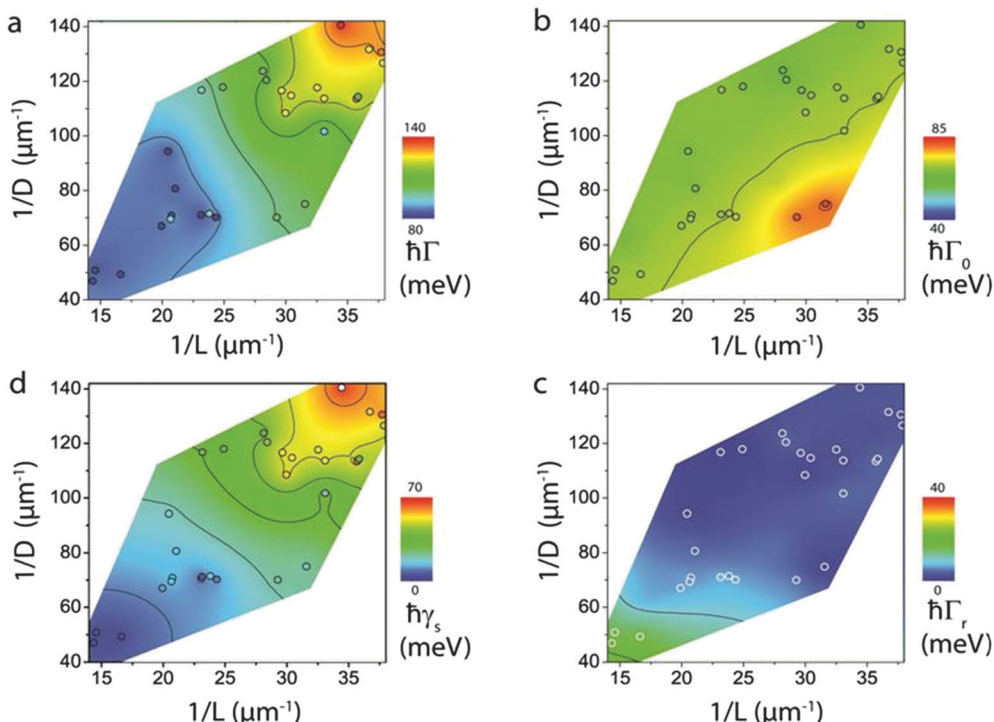


**Fig. 16** Spectral width of the longitudinal SPR of single Au@SiO<sub>2</sub> nanorods as a function of their inverse length  $L$  and diameter  $D$ . (a) Measured total width of the extinction spectra  $\Gamma$ . (b) Computed bulk contribution using eqn (16). (c) Radiative ( $\Gamma_r$ ) contribution computed using finite element modeling. (d) Deduced surface ( $\gamma_s$ ) contribution. The contributions deduced from measurements in different rods are shown as open dots (inner color indicates the measured/deduced width). Color maps interpolated to the whole  $(1/L, 1/D)$  region covered by the experiments are also presented with contours at fixed widths. Reprinted with permission from ref. 157 (Copyright 2013 American Chemical Society).

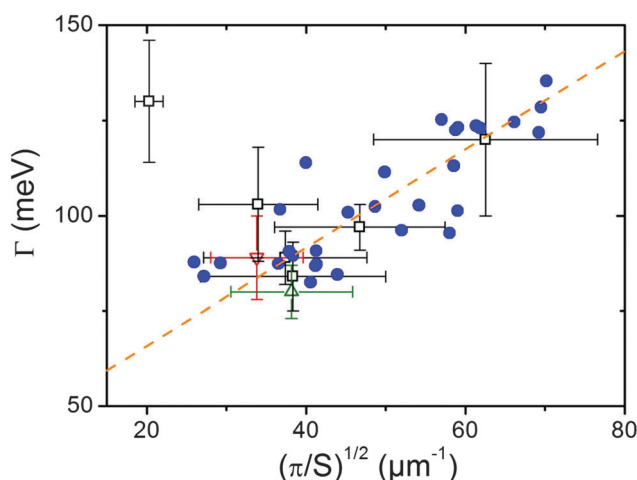


**Fig. 17** Measured longitudinal SPR width  $\Gamma$  of single Au nanorods (black squares,<sup>198</sup> green triangle,<sup>167</sup> red triangle<sup>112</sup> and blue circles<sup>157</sup>), plotted as a function of  $1/L_{\text{eff}} = (\pi/S)^{1/2}$ . The dashed orange line is a linear fit with a surface scattering coefficient  $A = 1.4$  (see text).<sup>157</sup> Nanorod sizes are estimated by optical size determination<sup>157</sup> or using mean sample dimensions<sup>112,167,198</sup> (size dispersion being shown by horizontal error bars, while vertical ones indicate the standard deviation of  $\Gamma$  for different single-particle measurements).

metallic nano-systems, due to the large electromagnetic interactions between metal nanoparticles separated by distances smaller or of the order of their size (*i.e.*, extension of the local

field associated to their dipolar SPRs). It permits to create giant local enhancement of the electromagnetic fields (for instance in the gaps between two nearby nanoparticles),<sup>16,201</sup> to modify the dipolar SPR spectra in a particle distance dependent manner,<sup>170,202</sup> and to induce additional resonances originating from multipolar SPRs for small separating distances.<sup>203,204</sup>

As the impact of electromagnetic interaction largely depends on the morphology and distance of the interacting particles, study of the optical response of an individual multi-component nano-object and precise characterization of its morphology is thus of central interest. This approach has been exploited to investigate multi-component metal-based nano-objects of different size, shape and composition: *e.g.*, pairs of nanoparticles of the same (homodimers) or different (heterodimers) materials,<sup>46,170,205</sup> or more complex nanostructures such as oligomers,<sup>206</sup> nanodolmens<sup>207</sup> and Fanoshells.<sup>208</sup> Most experiments were performed using scattering-based dark-field methods, and have been already extensively reviewed.<sup>180</sup> We will thus focus here on illustrating few key effects in homodimers and on recent investigation of heterodimers, also excluding recent studies of large plasmonic nanoclusters formed by the 3-dimensional assembly of a large number of nanoparticles with the goal of producing metafluids.<sup>209</sup> Note that the physical mechanisms underlying the optical response of a homodimer are similar to those for particle–substrate interaction, as the latter situation can be described as interaction of a particle with its image (Section 3.1.3).

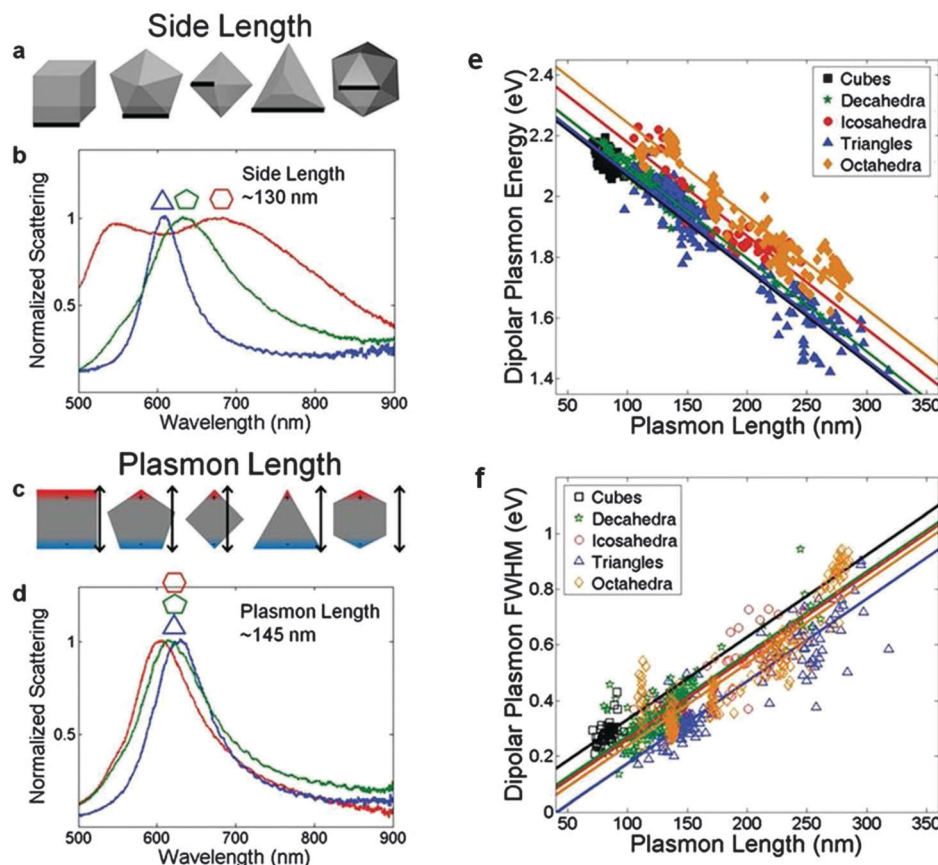


**Fig. 18** Comparison between the side length (defined in (a)) and plasmon length (defined in (c)) as descriptors of nanoparticle size for different shapes. Representative single-particle scattering spectra of Au triangles (blue), decahedra (green), and icosahedra (red) of similar side length (b) and plasmon length (d). Dipolar plasmon energy (e) and width (f) dependencies on the plasmon length. Adapted with permission from ref. 82. Copyright 2012 American Chemical Society.

Homodimers have been produced using electron lithography<sup>170,205,210</sup> (with typical nanoparticle sizes and separations larger than 50 nm and 10 nm, respectively; smaller gaps can be produced, but suffer from large interdimer dispersion<sup>210</sup>), DNA bonding,<sup>202,211,212</sup> random association in colloidal solution spin coating,<sup>213</sup> self or electrostatic assembly between chemically synthesized nanoparticles (30–100 nm size ranges, with separations down to nanometer<sup>46,211,214</sup>). For randomly oriented dimers constituted by two nanospheres, an important advantage of single-particle studies over ensemble ones is to permit analysis of the polarization dependence of the dimer optical response (as in the case of single elongated particles). It is a consequence of larger electromagnetic coupling between the component particles for parallel than perpendicular light polarizations relative to the dimer axis. This effect, analog of the polarization dependence induced by the presence of a substrate (Section 3.1.3), has for instance been shown for single gold<sup>103,170</sup> and silver<sup>211</sup> homodimers (Fig. 19). For small and identical component particles, reduction of the separating distance has been shown to induce a red shift of the dipolar SPR for parallel polarized light, as compared to orthogonally polarized light and isolated particles (Fig. 19), in agreement with the dipolar plasmon hybridization picture and numerical simulations.<sup>170,202,205,211,212</sup> These results were consistent with

those obtained in ensemble measurements of lithographed samples (with identically orientated dimers on the substrate).<sup>215</sup> The dependence of the scattering spectra on the particle distance was also demonstrated by changing the distance between the dimer constituents (pair of lithographed gold prisms) by manipulating them with an AFM tip.<sup>216</sup> The effect of an asymmetry in the size or in the shape of the constituting nanoparticles was investigated in the case of single material dimers and interpreted using the same theoretical approaches.<sup>204,211</sup>

For small separating distances, the optical spectra of dimers depend on the details of the morphology of their constituent particles, an effect that can be associated to activation on short distance of their multipolar interactions. This was demonstrated by performing precise TEM characterization of the shape of a silver nanocube pair and measuring its extinction spectrum by SMS.<sup>203</sup> For even smaller, subnanometric distances, electron tunneling between the component particles becomes possible and the dimer optical properties cannot anymore be described by a purely classical electromagnetic approach. This regime was investigated by approaching two 300 nm large gold nanospheres placed on two AFM tips and following the system conduction and optical scattering<sup>217</sup> (Fig. 20). For separating distances of the order of the inter-atomic distance in gold, the measured scattering spectra show a blue shift with distance reduction, in

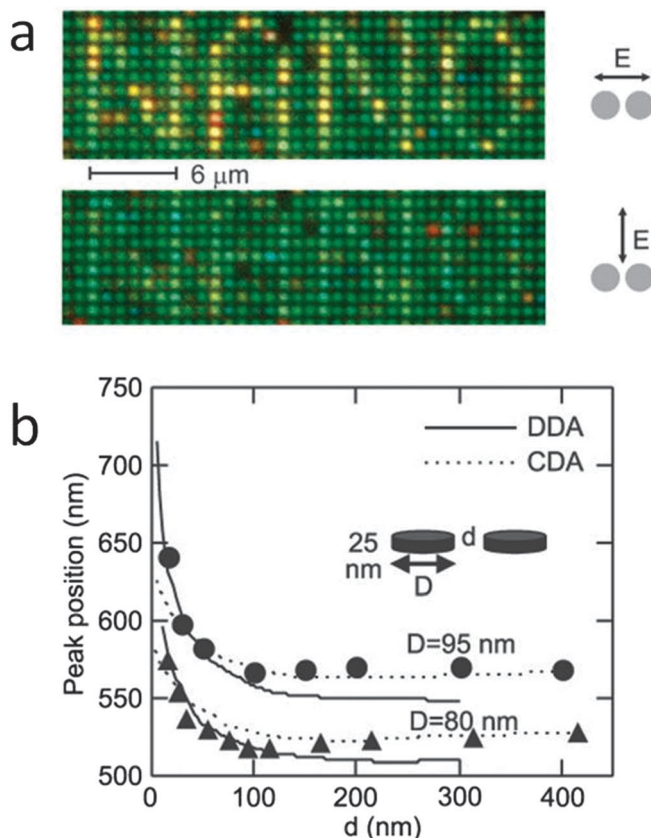


**Fig. 19** Dark-field images from an array of “identical” lithographed silver disks with a diameter of 80 nm and a height of 25 nm. (a) Text written with pairs of disks separated by 110 nm, and read with light polarized parallel or perpendicular to the particle pair axis (upper or lower image, respectively). (b) SPR spectral position of individual disk pairs measured by dark-field microscopy with parallel light polarization as a function of their edge separation  $d$  for two disk diameters:  $D = 80$  or 95 nm. The full and dotted lines show the results of discrete-dipole approximation (DDA) and coupled-dipole approximation (CDA) calculations, respectively. Reprinted with permission from ref. 170. Copyright 2005 American Chemical Society.

stark contrast with the red-shift observed for larger ones. This effect is qualitatively interpreted with models based on a simplified quantum-corrected approach,<sup>218</sup> or more precise ones involving time-dependent density functional theory (TDDFT) in the case of small nano-objects.<sup>219</sup>

Due to the difficulty of their controlled synthesis, hetero-dimers formed by two particles of different metals were experimentally investigated only very recently. They were formed by a gold and a silver sphere linked by DNA,<sup>211</sup> or by a silica-coated silver sphere and a gold sphere synthesized by electrostatic assembling.<sup>46</sup> Their polarization-dependent linear optical spectra were investigated by dark-field microscopy<sup>211</sup> and SMS,<sup>46</sup> respectively. As expected, the measured spectra show two resonances, close to the isolated silver and gold particle SPRs (Fig. 21). Their interaction in the dimer is indicated by a slight red-shift for light polarization parallel to the dimer axis as compared to the perpendicular one,<sup>211</sup> and by a large enhancement of the amplitude of the Au-like resonance, *i.e.*, of gold particle extinction (mostly absorption in the studied dimers) in the dimer as compared to the same isolated gold particle.<sup>46</sup>

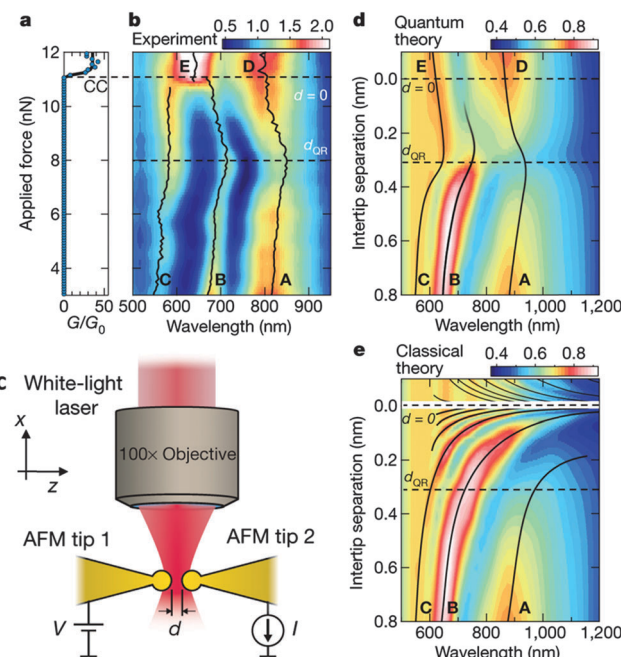


**Fig. 20** Simultaneous electrical conductance (a) and dark-field optical scattering (b) of closely spaced gold nanoparticles attached to tips (c). Increasing force is applied to the inter-tip cavity after snap-to-contact, conductive contact (CC) indicating  $d = 0$ , with onset of quantum regime at  $d_{QR}$ . Theoretical total scattering intensity from a tip–tip system including quantum mechanical tunneling (d) or using purely classical calculations (e). Adapted by permission from MacMillan Publishers Ltd: Nature (ref. 217), copyright 2012.

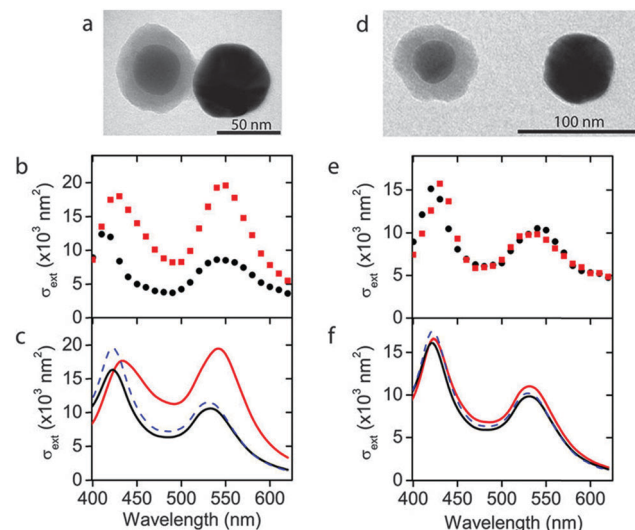


**Fig. 21** Measured (b) and computed (c) optical extinction spectra of single Au-Ag@SiO<sub>2</sub> heterodimers together with their TEM images (a). The incident light is polarized parallel (red squares and lines) or orthogonal (black circles and lines) to the dimer axis. The spectra were computed using the TEM measured sizes. The dashed blue line is the sum of the computed extinction cross-sections of isolated Au and Ag@SiO<sub>2</sub> nanospheres with the same sizes. (d–f) Same as (a–c) for a pair of quasispherical Ag@SiO<sub>2</sub> and Au particles separated by 50 nm. Reprinted with permission from ref. 46. Copyright 2013 American Chemical Society.

These results were in agreement with theoretical numerical models, the red shift of the Ag-like resonance (not predicted by the plasmon hybridization model<sup>179</sup>) being induced by a Fano effect, *i.e.* resonant interaction between a discrete resonance (the Ag-like SPR) and a spectrally overlapping continuum of states (the interband transitions of gold).<sup>180,220</sup> They reflect large changes of the electromagnetic field distribution in and around the particle, leading in particular to giant field enhancement in the interparticle region.<sup>46,221</sup> However, these spectral and amplitude effects were found to depend on the studied dimer, and can thus be interpreted precisely only by determining its morphology as done by TEM (Fig. 21).<sup>46</sup> In particular, this analysis clearly showed that the spectral red shift signature of the electromagnetic coupling effect could disappear or even be reversed in dimers formed of slightly elliptical nanoparticles, due to competition between shape and electromagnetic coupling effects.

Particle interaction with its image has also been studied for a single particle on a metallic substrate, with additional phenomena due to coupling of the particle localized SPR with the propagating surface plasmon polaritons (SPPs) of the substrate.<sup>180,222</sup> This was experimentally investigated for single gold and silver particles on a gold film, as a function of their relative distance adjusted by a spacing layer, or for gold particles partly embedded in the film.<sup>223–225</sup> Strong, distance-dependent red shifts of SPR resonance were observed in the scattering spectra of nanoparticles as they were approached at a distance of the substrate below their size, in agreement with theoretical modeling.<sup>226</sup> Plasmon resonance splitting was also observed in

some single particle scattering spectra, and attributed to a lift of degeneracy between horizontal and vertical plasmon modes,<sup>224</sup> similar to the dielectric substrate case (Section 3.1.3). Very recently, these investigations have been extended to conductive spacers as a single layer of graphene.<sup>227</sup>

## 4. Linear optical properties of semiconductor nano-objects and carbon nanotubes

Semiconductor nano-objects are very promising for many applications such as in nano-electronics (transistors, nanoscale logic circuits), bio-labelling, photodetectors, and solar cells. While their luminescence has been intensively investigated and is an efficient tool for their detection and study at the single nano-object level,<sup>1,26,35</sup> study of the absorption of a single particle is only emerging. Detection and investigation of the absorption and extinction of single quantum dots has been demonstrated using photothermal<sup>119</sup> and SMS<sup>228</sup> methods, respectively. Similar to metal nanoparticles, quantitative extinction spectroscopy using SMS is particularly interesting and has been recently applied to investigation of II-VI semiconductor nanowires and semiconductor carbon nanotubes.

### 4.1. CdSe semiconductor nanowires

The extinction spectra of single CdSe nanowires were measured using PHI,<sup>124</sup> and, more quantitatively, using SMS<sup>113</sup> (Fig. 22a).

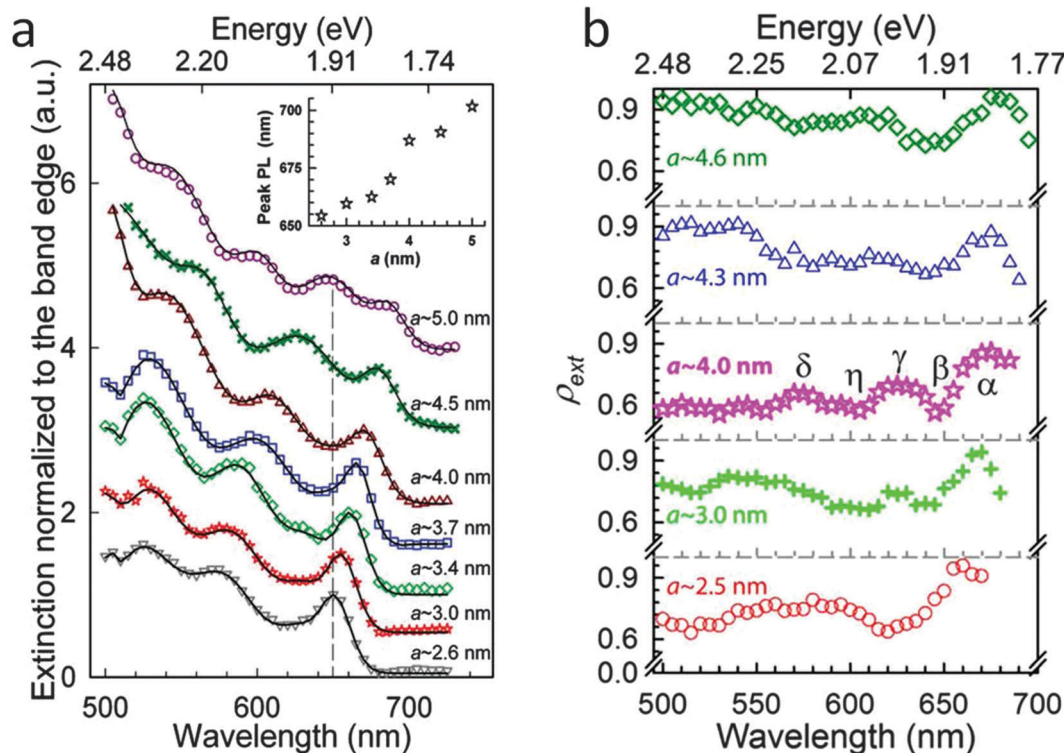


Fig. 22 (a) SMS measured extinction spectra of single CdSe nanowires with radius ranging from 2.6 to 5 nm. The inset shows the corresponding luminescence peak position as a function of the nanowire radius. (b) Anisotropy factor ( $\rho_{ext}$ ) spectra for several different individual CdSe nanowires. Adapted with permission from ref. 113 (Copyright 2011 American Chemical Society) and ref. 229 (Copyright 2012 American Chemical Society).

For SMS-investigated nanowires, with diameters in the 5–10 nm range,<sup>113</sup> extinction is dominated by absorption, and the measured amplitudes of absorption cross-sections per unit length were found to be consistent with those computed using classical laws of electromagnetism, and, surprisingly, the dielectric constants of bulk CdSe.<sup>113,229</sup> Single particle spectra show several excitonic peaks, which, as expected, blue shift with decreasing nanowire radius. Their spectral positions have been found to be in agreement with those computed using a six-band kp model for CdSe absorption<sup>230</sup> modified to include Coulombic effects. The polarization anisotropy  $\rho_{\text{ext}} = (\sigma_{\text{ext}}^{\parallel} - \sigma_{\text{ext}}^{\perp})/(\sigma_{\text{ext}}^{\parallel} + \sigma_{\text{ext}}^{\perp})$  of the extinction cross-sections for incident light polarized along ( $\parallel$ ) or orthogonally ( $\perp$ ) to the nanowire axis of single CdSe nanowires was also measured<sup>113,229</sup> (Fig. 22b). Its complex wavelength dependence has been interpreted as a consequence of classical dielectric confinement effects<sup>231</sup> but also, at specific wavelengths, of different efficiencies of optical transitions due to confinement-induced mixing of valence band states. This polarization signature (*i.e.* strong difference in the optical response for light polarized parallel and perpendicular to the axis of elongated nano-objects) was exploited to investigate nanorods and nanowires by polarization-modulation microscopy (Section 2.2.5) in extinction experiments,<sup>66</sup> or through a polarization-modulated Rayleigh scattering spectroscopy technique, which was shown to reveal the electronic structure spectral features of GaAs and InP nanowires with a high signal-to-noise ratio and spectral resolution.<sup>232</sup>

## 4.2. Single-wall carbon nanotubes

Comprehension and characterization of the optical absorption processes in single-wall carbon nanotubes (SWNTs), and of the way they are modified by their environment, are crucial both for their applications and their investigation by optical means, and, more generally, for fundamental understanding of light-matter interaction in quasi one-dimensional nanomaterials. Due to the large heterogeneities of the carbon nanotube structural parameters in most synthesized ensembles, investigation of single identified nanotubes is particularly relevant. It has been largely developed during the last few years using photoluminescence or Raman and Rayleigh scattering.<sup>83,233,234</sup> Optical imaging and identification of individual carbon nanotubes have thus been performed, yielding information on their excitonic resonant energies and linewidths correlated with their structure and chirality. These investigations have been already reviewed,<sup>235,236</sup> and we will focus here on quantitative studies of the absorption cross-section of a carbon nanotube which is still an open question.

The absorption cross-section values of single wall carbon nanotube (SWNT) were first indirectly determined at specific wavelengths using luminescence, thermal, or Rayleigh scattering techniques.<sup>237–240</sup> Imaging and direct measurement of the absorption cross-section of SWNTs grown on an opaque silicon substrate was subsequently achieved for few discrete wavelengths using the spatial modulation technique in reflective configuration (R-SMS) (Fig. 23).<sup>65</sup> Correlation with Raman spectroscopy permits

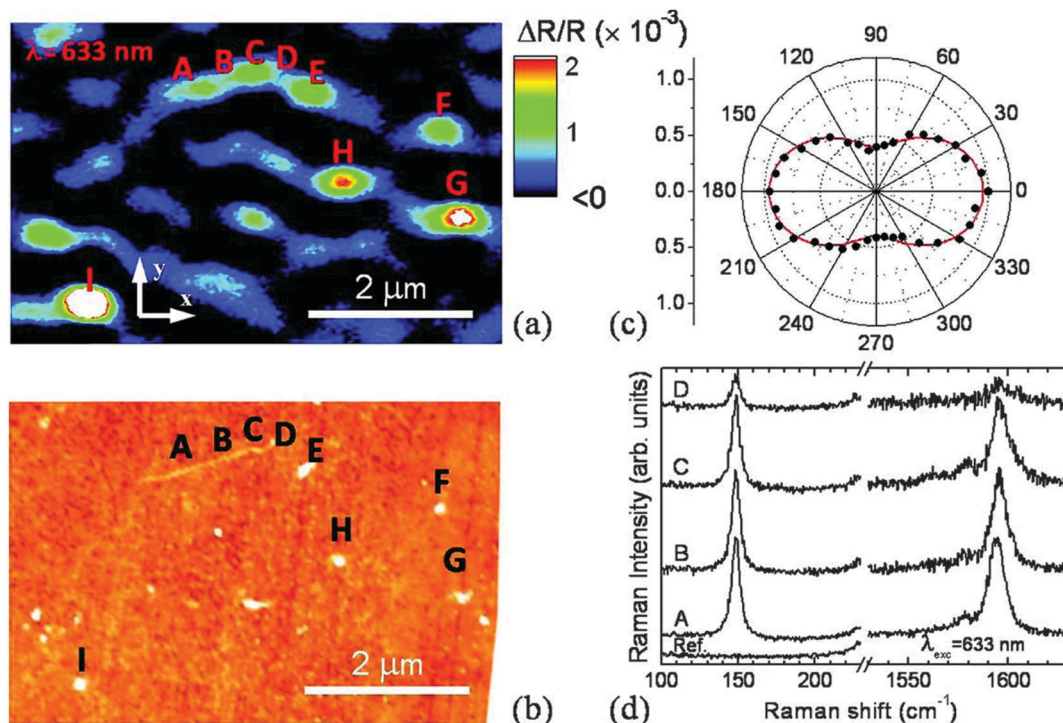


Fig. 23 R-SMS (a) and AFM (b) images of a single wall carbon nanotube (SWCNT) with a diameter of 1.65 nm on a SiO<sub>2</sub>/Si substrate. (c) Light-polarization-dependent R-SMS signal recorded from point B of the nanotube. (d) Raman spectra measured at different spots (A–D on the R-SMS image) showing the CNT radial breathing mode (RBM) at 148 cm<sup>-1</sup> and its G-band peak (tangential modes) around 1595 cm<sup>-1</sup>. A reference spectrum from an “empty” area of the sample is also shown. Adapted with permission from ref. 65. Copyright 2012 American Chemical Society.

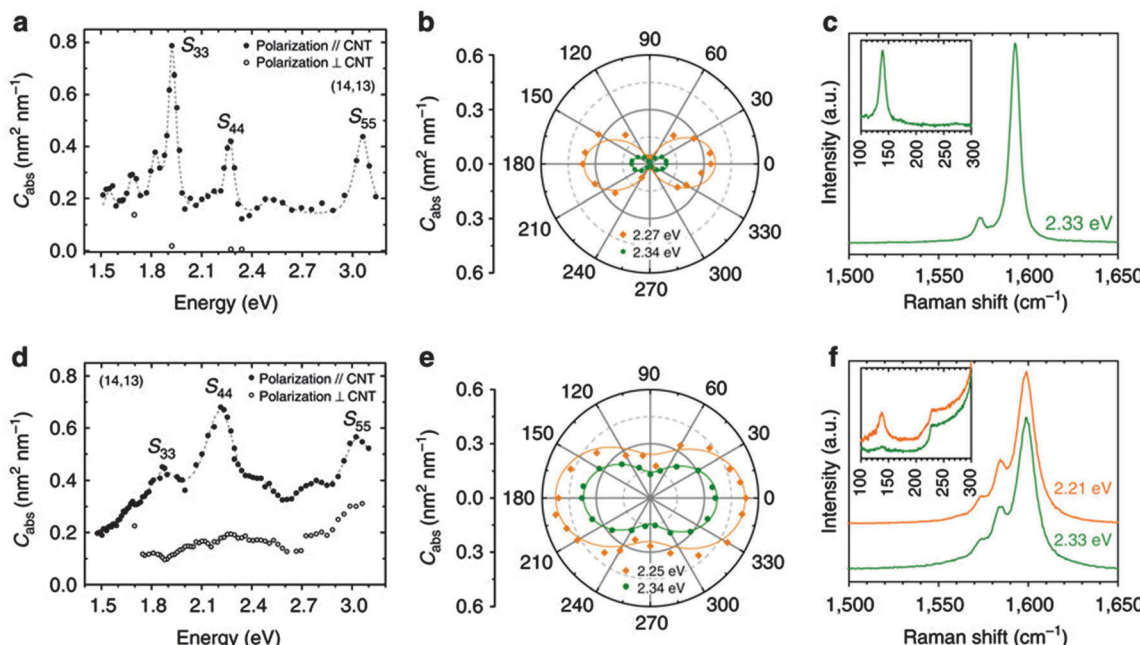


Fig. 24 SMS measured optical extinction spectra (a), light polarization dependence (b) and Raman spectra (c) of an individual single-wall carbon nanotube with a diameter of 1.83 nm suspended over a trench. (d–f) Same as (a–c) for one extremity of the same nanotube, supported on a silicon substrate, measured by R-SMS. Adapted by permission from MacMillan Publishers Ltd: Nature Communications (ref. 116), copyright 2013.

identification of the investigated semiconductor SWNT, with diameter in the 1.6 nm range, whose polarization dependent absorption was also determined.<sup>65</sup> This first study opened the way to quantitative and direct characterization of the optical absorption of carbon nanotubes using SMS and R-SMS.<sup>65,107,116</sup>

Recently, it has been extended to optical detection and investigation of partially suspended SWNT, over the visible–near infrared spectral range (Fig. 24).<sup>116</sup> The full optical spectral features (absorption energies, amplitudes and spectral widths) of different excitonic transitions were thus precisely determined for different semiconducting SWNTs identified in size and chirality by correlation with Raman spectroscopy. In particular the oscillator strength of different excitonic resonances and their dependence on the type of semiconducting nanotube were determined and found to be consistent with recent theoretical studies.<sup>241</sup> A non-resonant absorption background was also detected and its cross-section determined and connected to the graphene optical conductance.<sup>242,243</sup>

Combining SMS and R-SMS, the same SWNT was investigated either suspended (on its central part over a trench, Fig. 7c) or deposited (on its extremities supported on the silicon substrate) permitting direct investigation of the impact of the substrate on its optical response. A large broadening of the excitonic resonances, with increase of oscillator strength, as well as a stark reduction of the polarization anisotropy due to SWNT–substrate interaction has thus been evidenced (Fig. 24). This opens the way to quantitative modeling of nano-object–substrate interaction, a major issue in single nano-object study (see Section 3.1.3) and for applications.

## 5. Ultrafast spectroscopy of single nano-objects

The optical response of a nano-object can be actively modified and controlled by modifying its dielectric function. This can be achieved optically with a light pulse, exploiting the optical nonlinearities of the constituent material, and in particular the large ones of metals or semiconductors. Using femtosecond pulses, this opens the way to ultrafast active control of light propagation or transmission,<sup>244,245</sup> and to fundamental investigation of ultrafast material properties. In this context, time-resolved spectroscopy has been extensively used, first in metal films<sup>153,246–248</sup> and, subsequently, in metal nanostructures.<sup>2,3,8,47,155,158–160,249–256</sup> It has provided information on electronic motion coherence losses or SPR polarization decay,<sup>155,250–252</sup> on electron energy redistribution in nano-objects<sup>47,158–160,253</sup> (electron-electron, electron-lattice and electron-surface scattering), on their acoustic vibrations<sup>2,3,47,254,255</sup> and on nanoscale metal-environment energy exchanges.<sup>8,256</sup>

Recently, these studies have been extended to single nanoparticles, permitting, similarly to the linear plasmonic investigations (Section 3.1), quantitative comparison of the experimentally measured nonlinear optical response with theoretical models and thus precise determination of the physical origins of the third order nonlinearity in plasmonic nano-objects.<sup>48–52,128,257</sup> In this context, femtosecond pump-probe spectroscopy, based on illumination of a single nano-object with a femtosecond pump pulse and monitoring of the induced change of its optical response by a second time-delayed probe pulse, has been most

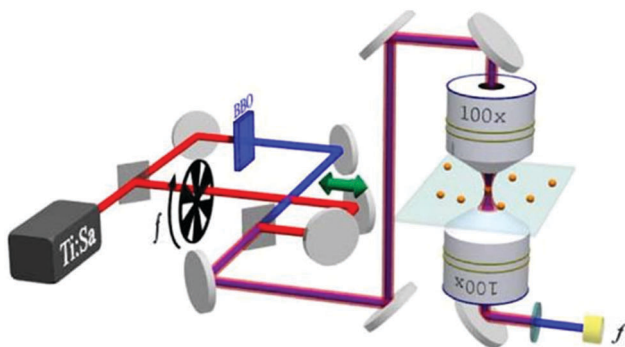


**Fig. 25** Schematic setup for two-color time-resolved pump–probe spectroscopy using a near-infrared beam from a Ti:sapphire femtosecond oscillator. The initial beam is split into two parts used as a pump and probe, the latter being frequency-doubled in a BBO crystal. The pump beam intensity is modulated using a mechanical chopper and the pump–probe delay is controlled using a translation stage inserted on the pump path. Probe transmission changes induced by the pump beam are demodulated at frequency  $f$  by lock-in detection, after spectral filtering of the pump beam.

largely used (by fixing the pump–probe delay, it can also be applied to detect the presence of a nano-object, using a confocal scan of the pump and probe spots over the sample). Depending on the probe wavelength, the different physical relaxation processes following electronic photoexcitation of a nano-object by absorption of the pump pulse can then be monitored on different timescales: energy exchange within the object among electrons and with the ionic lattice, launching and damping of object vibrations (Section 6), and heat transfer to its environment (typically picoseconds, tens of picoseconds, and hundreds of picoseconds, respectively<sup>2,3,8,159,258</sup>). Experiments were performed by detecting the transient pump-induced change of either probe scattering<sup>51,259</sup> or extinction.<sup>48,52,260</sup> They use high stability and high repetition rate tunable laser sources (as Ti:sapphire femtosecond oscillators, possibly combined with frequency conversion schemes, such as second or third harmonic generator or optical parametric oscillator), and modulation of the pump beam at high frequency with lock-in detection of the pump-induced change of probe scattering or extinction (Fig. 25).

In extinction-based experiments, the transmitted probe beam is recollected after interaction with the nano-object. For a small (as compared to the beam spot size) nano-object placed at the center of the pump and probe spots, the pump pulse induces a transmission change  $\Delta T/T$  at probe wavelength  $\lambda_{\text{pr}}$  given by the change of the extinction cross-section  $\Delta\sigma_{\text{ext}}$  (neglecting, as for linear spectroscopy, change of the collected scattered light for small enough nano-objects):

$$\frac{\Delta T}{T}(\lambda_{\text{pr}}, t) \approx -\frac{\Delta\sigma_{\text{ext}}(\lambda_{\text{pr}}, t)}{S_{\text{pr}}} \quad (19)$$

where  $t$  is the pump–probe delay and  $S_{\text{pr}}$  the probe spot size (with  $S_{\text{pr}} = \pi w^2/2$  for a Gaussian probe beam of intensity waist  $w$  or full-width at half-maximum  $d_{\text{FWHM}} = w\sqrt{2\ln 2}$ ).<sup>48,52</sup> As  $S_{\text{pr}}$  can be experimentally measured, the time-dependent change of  $\sigma_{\text{ext}}$  can then be quantitatively determined.<sup>48</sup> It reflects that of

the dielectric constant  $\varepsilon$  of the material forming the particle, induced by the pump pulse of wavelength  $\lambda_{\text{pp}}$ . In the small perturbation regime, it can be written as:

$$\Delta\sigma_{\text{ext}}(\lambda_{\text{pp}}, \lambda_{\text{pr}}, t) = a_1|_{\lambda_{\text{pr}}} \Delta\varepsilon_1(\lambda_{\text{pp}}, \lambda_{\text{pr}}, t) + a_2|_{\lambda_{\text{pr}}} \Delta\varepsilon_2(\lambda_{\text{pp}}, \lambda_{\text{pr}}, t) \quad (20)$$

The optical nonlinear phenomena are reflected in the changes of the real and imaginary parts,  $\Delta\varepsilon_{1,2}$ , of the metal dielectric function  $\varepsilon$ , due to the intrinsic optical nonlinearity mechanisms of the material forming the particle.<sup>153,159,261</sup> The  $a_{1,2}$  coefficients are given by  $a_{1,2} = \partial\sigma_{\text{ext}}/\partial\varepsilon_{1,2}$ , and are thus set by the linear extinction properties of the particle (for instance, they can be calculated using eqn (13) for a nanoellipsoid, or numerically for complex shapes<sup>48</sup>). For metallic nanoparticles, these coefficients are enhanced and strongly dispersed for wavelengths around the particle SPRs. The intrinsic nonlinearity is then enhanced by plasmonic effects in metal nano-objects, which actually reflects the consequence of local field enhancement in the particle around its SPR wavelength.<sup>48,261</sup>

In most experiments, the amplitude of  $\Delta\varepsilon$  and thus of  $\Delta T/T$  is set by the excess energy injected in the electrons and/or by the density of photoexcited carriers at the probing time  $t$  after photoexcitation by the pump pulse, permitting to follow their time evolution. Knowledge of the absolute absorption cross-section of a single particle at the pump wavelength thus permits to quantify this excitation, and thus its nonlinear response. This has been done by measuring the absorption cross-section of optically identified single objects deposited on glass by SMS and performing pump–probe spectroscopy measurement on the same particle.<sup>48,52</sup> Electron-lattice energy exchange kinetics has thus been precisely investigated in single silver nanospheres (in the 20–30 nm size range). Its dependence on the absorbed energy has been quantitatively determined and found to be in agreement with predictions of the two temperature model (Fig. 26).<sup>52,262</sup> The spectrally and temporally dependent response of a gold nanorod around its longitudinal SPR has been quantitatively interpreted in terms of enhancement by the plasmonic effect of the bulk metal nonlinearity (Kerr-like nonlinearity due to electron heating, up to a few picoseconds, and by lattice heating on a longer time-scale<sup>48</sup>) (Fig. 27). These investigations also permit to connect the nonlinear third order hyper-polarizability of a single nano-object to third order nonlinear susceptibility of an ensemble forming a composite material, opening many possibilities for predicting the optical nonlinearity of plasmonic devices.<sup>48</sup>

The time-dependent changes of both the real and imaginary parts of  $\varepsilon$  contribute to the time-dependent change of  $\sigma_{\text{ext}}$  measured in transient extinction spectroscopy (eqn (20)). As for linear spectroscopy, these contributions can be separated using interferometric techniques, where a reference beam is used to access phase information. Four-wave mixing microscopy experiments with heterodyne detection were developed to extract the ultrafast changes of the complex polarizability of single spherical gold nanoparticles (smaller than 40 nm) at their SPR wavelength.<sup>43,263</sup>

Very recently, pump–probe microscopy techniques have been extended to individual metallic (Ag) and semiconductor (Si, CdSe, CdTe) nanowires down to 10 nm diameter<sup>127,128,264,265</sup>

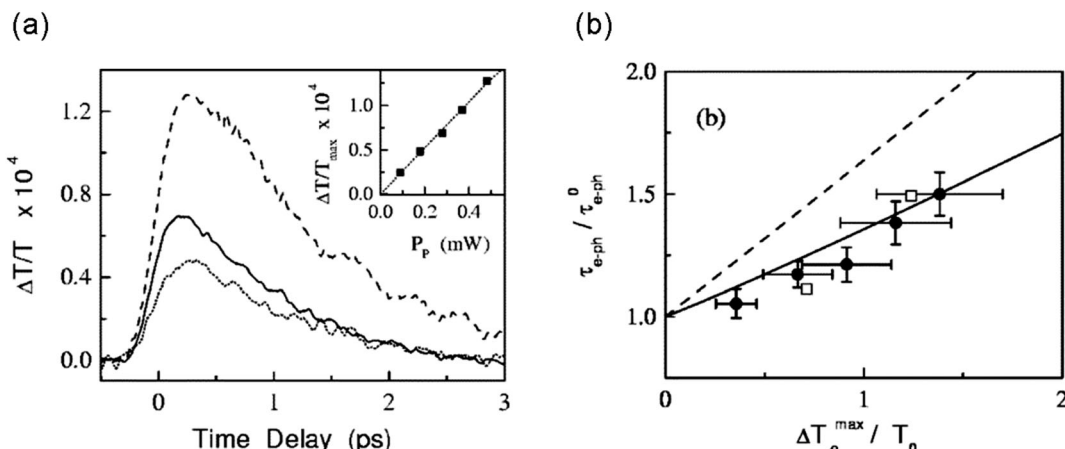


**Fig. 26** (a) Pump power dependence of the ultrafast transmission change  $\Delta T/T$  measured using pump–probe extinction spectroscopy in a single 30 nm Ag nanoparticle. The inset shows the measured linear dependence of the maximum signal amplitude on the pump power. (b) Measured electron energy transfer time to the lattice  $\tau_{e\text{-}ph}$  normalized to the low pump power one  $\tau_{e\text{-}ph}^0$  as a function of the initial electronic temperature increase  $\Delta T_e^{\max}$  due to pump pulse absorption. Adapted with permission from ref. 52. Copyright 2006 American Chemical Society.

and chirality identified individual single-wall carbon nanotubes.<sup>130,266</sup> Correlation of single particle transient absorption investigations using morphological characterization techniques (optical with SMS, TEM, SEM, photoluminescence or Raman spectroscopy) permits detailed interpretation of the measured responses and comparison with theoretical models. The information obtained on carrier relaxation kinetics and carrier-phonon scattering has thus yielded new insight into the influence of charge carrier trapping induced by surface defects in semiconductor nanowires<sup>127,264,265,267</sup> and the impact of the substrate, by comparing the results for suspended and deposited carbon nanotubes.<sup>130,266</sup>

Time-resolved scattering-based measurements use a similar approach, the probe light then monitoring the transient change of a nano-object scattering induced by a pump-pulse. A signal proportional to  $\Delta\sigma_{\text{scat}}$  is thus recovered, which can be connected, as  $\Delta\sigma_{\text{ext}}$  (eqn (20)), to the induced changes of the metal dielectric function  $\Delta\epsilon_{1,2}$ .<sup>51,259</sup> Transient polarized scattering was largely exploited and demonstrated to be a powerful tool for investigating carrier dynamics in single semiconductor nanowires with diameters below 100 nm.<sup>259</sup> In these experiments the pump pulse modulated by a mechanical chopper excites the nanowire. A probe pulse, whose polarization is modulated to avoid background contributions,<sup>232</sup> measures the pump-induced change between the parallel and orthogonal back scattering amplitude of the wire. Measurements performed as a function of the probe wavelength provide detailed information on the time evolution of the density and temperature of the electrons and holes after photoexcitation, as shown in the case of a single GaAs-AlGaAs core–shell nanowire. The results were compared to a model including transport, recombination, and cooling through optical and acoustic phonon emission.<sup>232,259</sup>

Ultrafast investigations combined with microscopy techniques have permitted exploration of other important physical phenomena in single nano-objects, as the dynamics of magnetization in ferromagnetic nanodots (with sizes > 200 nm) over a

broad temporal scale ranging from 100 fs to 1 ns, or dynamical imaging of the magnetization for a fixed delay between the pump and probe pulses.<sup>268,269</sup>

## 6. Acoustic vibrations of nano-objects

As their optical response, size reduction strongly modifies the acoustic response of nano-objects. In the low frequency domain, they exhibit discrete vibrational modes whose characteristics depend on the object composition, morphology, and environment. The interest they have motivated is due to both possible applications (*e.g.*, design of ultrasensitive mechanical mass sensors or high frequency mechanical oscillators<sup>254,270,271</sup>) and fundamental questioning, regarding for instance acoustic interactions or laws of elasticity at the nanoscale. Optical spectrally (Raman) and temporally resolved (pump–probe) spectroscopies have been one of the main source of information on nanoscale vibrations, due to their ability to detect vibrational modes without contact in different environments.<sup>2,272,273</sup> Most investigations have been performed on ensembles of different types of nano-objects, permitting good understanding of the effects of size,<sup>2,40,255,272–274</sup> shape,<sup>21,22,275–277</sup> crystallinity<sup>21,112,277,278</sup> and encapsulation<sup>279–281</sup> on vibrational periods for size down to  $\approx 1$  nm.<sup>254</sup>

Much less information has been obtained on the homogeneous linewidth (or damping rate in the time domain) of these modes due to external and internal acoustic energy transfer processes. It is however a key parameter for application as it defines the mode quality factor, and also raises fundamental questions on the involved energy exchange mechanisms at the nanoscale. It is usually masked in ensemble measurements due to inhomogeneous line broadening (or interparticle dephasing), reflecting nano-object size and shape dispersions (similarly to SPR or exciton inhomogeneous line broadening in metal or semiconductor nanoparticles, Fig. 8b).<sup>255</sup> They have thus been

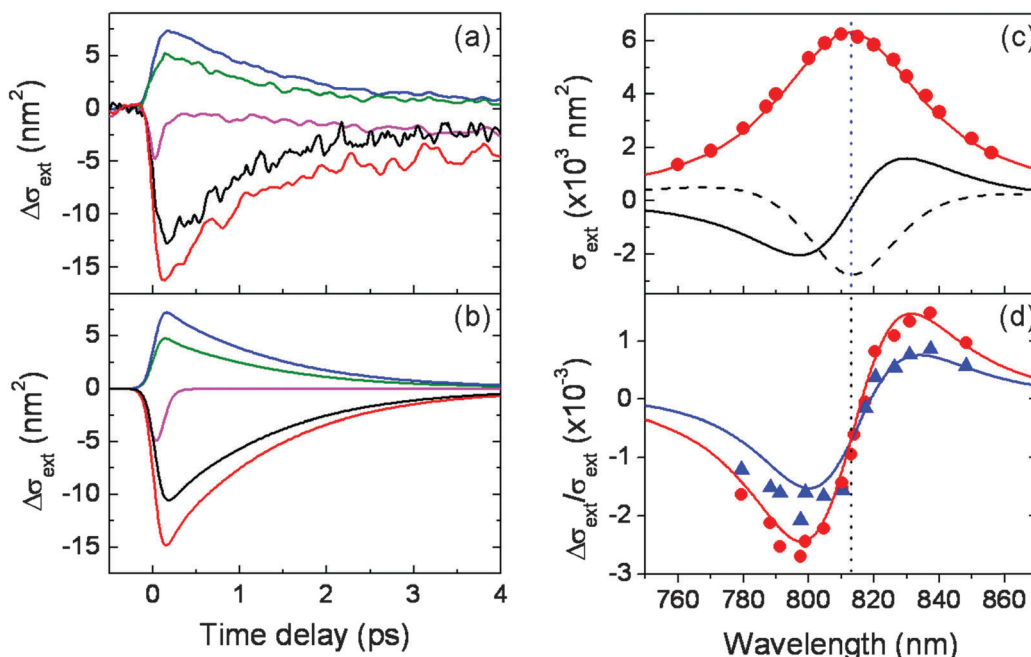


**Fig. 27** Experimental (a) and computed (b) time-dependent extinction cross-section changes measured for a single gold nanorod at different probe wavelengths around its SPR: from top to bottom  $\lambda_{\text{pr}} - \lambda_{\text{SPR}} \sim +30, +40, 0, -30 and  $-20 \text{ nm}$ . (c) SMS measured extinction cross-section  $\sigma_{\text{ext}}$  spectrum (dots) of the investigated nanorod, and its numerical fit (full red line) using the finite element method. The black full and dashed lines are the computed derivatives  $a_{1,2} = \partial\sigma_{\text{ext}}/\partial\epsilon_{1,2}$ . (d) Ultrafast extinction cross-section changes  $\Delta\sigma_{\text{ext}}$  measured for pump–probe delays of 0 fs (triangles) and 200 fs (dots), and computed interband contribution for the same time delays (full lines) using eqn (20). Adapted from ref. 48 (Copyright 2011 by The American Physical Society).$

analyzed only in very narrow size and shape distribution nanospheres in glass<sup>2</sup> and nano-bipyramids in liquid.<sup>22</sup> Both studies were performed using time-resolved femtosecond spectroscopy. This is based on coherent launching of the vibrations of particles by their ultrafast heating by a pump pulse, and direct time-domain monitoring of their oscillation with a time-delayed probe pulse following the induced modulation of their optical properties. It thus permits determination of vibrational mode periods and full decay rates (reflecting both homogeneous and

inhomogeneous contributions) (Fig. 28).<sup>281–285</sup> Inhomogeneous effects can be suppressed by investigating a single nanoparticle, yielding access to the homogeneous damping rate (Fig. 28).

Apart from application of Raman spectroscopy to identification of single carbon nanotubes,<sup>40,236</sup> which will not be reviewed here, most investigations of the acoustic modes of single nano-objects have focused on analysis of their damping, as illustrated below in the case of metal nanoparticles. They have first been performed on single gold nanoparticles with sizes down to 50 nm

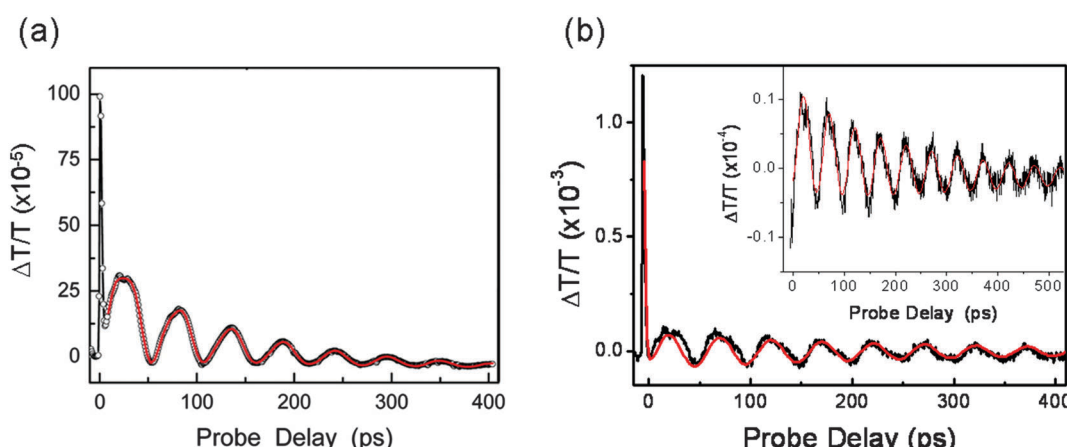


**Fig. 28** Time-resolved pump–probe transmission change signals measured in the extinction geometry for (a) an ensemble of gold nano-bipyramids in aqueous solution and of a single nano-bipyramid (b) from the same solution. The oscillating contribution to the time-resolved signal is enlarged in the inset. Panel (a) reprinted with permission from ref. 300. Copyright 2013 American Chemical Society.

using a time-resolved pump–probe interferometric technique.<sup>49,260</sup> The same pump–probe method as for investigation of the optical nonlinearity and electron kinetics of a nano-object, *i.e.*, time-domain extinction change spectroscopy (Section 5), was further used and exploited to investigate single particles with different morphologies and environments.<sup>53,173,286–288</sup>

As in ensemble measurements,<sup>2,272,281</sup> the time-resolved vibrational response of nanoparticles is usually dominated by the lowest frequency acoustic mode inducing a change in their volume (*i.e.*, breathing mode for a sphere).<sup>49,287,289</sup> The mode periods were measured in single gold and silver spheres<sup>289,290</sup> and in single various non-spherical single nano-objects: gold prisms,<sup>53</sup> dumbbells,<sup>287</sup> nanorods<sup>286</sup> and nanowires,<sup>288</sup> silver nanocubes<sup>54</sup> and nanowires<sup>173</sup> and semiconductor nanowires.<sup>127</sup> They were found to be in good agreement with theoretical calculations based on continuum mechanics, *i.e.*, assimilating the nano-object to an elastic body and using bulk elastic constants, confirming the results of the ensemble measurements mentioned above. These agreements have been obtained by either using the mean size and shape of the particles, or individually characterizing their morphology using SEM or TEM.<sup>286,287,289</sup> Correlation with electron microscopy also permits determination of the object crystalline structure and to evidence the role of crystalline anisotropy on the vibrational modes of elongated objects (*e.g.*, gold rods<sup>286</sup>). Though in most experiments the objects were deposited or lithographed on a substrate

(Fig. 29a), the latter has been usually found to slightly influence the measured mode period (except in the case of nanorods<sup>286</sup>), consistently with the weak influence of the environment shown in ensemble measurements.<sup>2,7,255</sup>

In contrast, the environment dramatically influences the homogeneous damping rate of vibrational modes, which is to a large extent determined by acoustic energy transfer from a nano-object to its environment.<sup>7,47,291–293</sup> Damping is thus highly sensitive to its nature and elastic properties (*via* the acoustic impedance mismatch between the particle and matrix material,<sup>7,294</sup> and, for small nanoparticles in liquid environments, viscosity<sup>22,292</sup>), and to its mechanical contact with the particle.<sup>282</sup> This effect, qualitatively observed in ensemble measurements (comparing data in glass or liquid environment),<sup>2,22,255</sup> has been quantitatively addressed by comparing the vibrations of deposited (gold rings<sup>295</sup> or nanorods,<sup>296</sup> with statistical comparison) or suspended (gold nanowire,<sup>288</sup> comparison on the same wire) nano-objects in air and liquid. In the case of a suspended nanowire, the damping rate due to energy transfer to the liquid environment can be computed and has been found to be in good agreement with the measured one, also showing the negligible role played by viscosity effects for about 100 nm wide nanowires.<sup>288</sup> Consistently, larger quality factors were also observed for single gold nano-objects as compared to silver ones, as the acoustic impedance of gold is larger.<sup>47</sup>

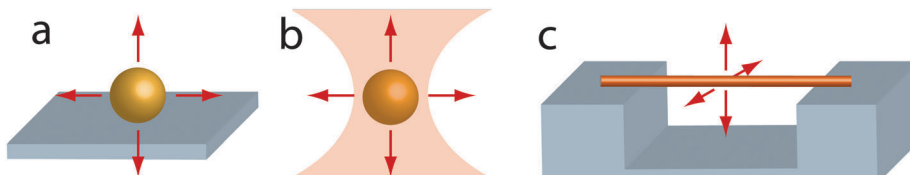


Fig. 29 Different configurations used in single-nano-object time-resolved experiments: (a) deposited, (b) optically trapped and (c) suspended object. Optical trapping is performed in liquids, while nano-objects in (a) and (c) can be left in air or immersed in a liquid.

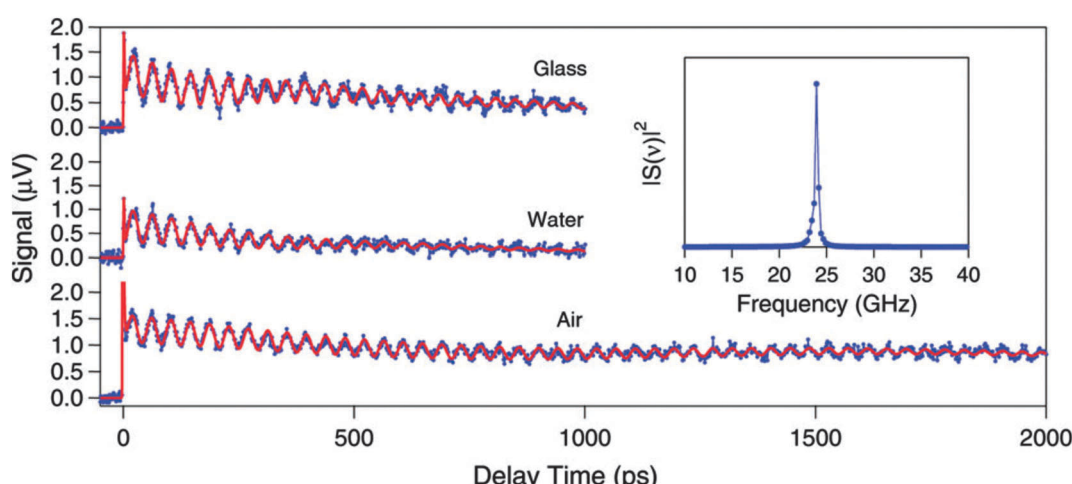


Fig. 30 Transient extinction change measured for a gold nanowire deposited on a glass substrate (top trace) and suspended over a trench in water (middle trace), and in air (bottom trace). The inset shows the Fourier transform of the trace in air. The single peak at 24 GHz corresponds to the breathing mode of the nanowire. Reprinted from ref. 288 with permission from the PCCP Owner Societies.

Damping modeling is more complex in the presence of a substrate, as it leads to an asymmetric particle environment and to another energy damping channel due to particle–substrate mechanical coupling. However, measured homogeneous damping times  $\tau$  of the acoustic vibrational modes of different nano-objects deposited or lithographed on a substrate (gold nanospheres,<sup>42</sup> nanoprisms,<sup>53</sup> nanorods<sup>286,290</sup> and nanowires<sup>288</sup> and silver nanocubes<sup>54</sup> and nanowires<sup>54,173</sup>) show large variations from object to object. No systematic correlation with the measured period was observed, leading to large variations in the quality factors  $Q = \pi\tau/T$  for different objects originating from the same solution, and for different vibration modes and nano-object shapes. It was ascribed to the variation of the environment and mechanical contact (*e.g.*, due to the delamination effect for the lithographed object, or the presence of ligands and residual solvent for spin-coated ones<sup>47,53</sup>). This effect was particularly important for synthesis of gold nano-prisms by nanosphere lithography, evaporation of gold onto a glass substrate leading to poor and variable mechanical contact.<sup>53</sup>

These fluctuations have stimulated experiments on single nano-objects in more homogeneous and better defined environments. This was achieved by optical trapping in liquids (for gold nanospheres and nanorods<sup>290</sup>, Fig. 29b) or, for long objects, by their suspension upon a trench in air (gold nanowire,<sup>288</sup> Fig. 29c and 30). As expected, smaller decay rates (as compared to those for deposited particles with liquid or air environments, respectively) were observed (Fig. 30), stressing the impact of the substrate. However, their values exceed the computed ones and vary between particles,<sup>288,290,295,296</sup> an effect particularly clear in the case of a nanowire in air for which almost no acoustic energy transfer to the environment is expected.<sup>288</sup> As suggested in ensemble measurements,<sup>22</sup> this effect indicates an inherent contribution to the damping (*i.e.*, not due to energy transfer to the surrounding media) with, because of its particle dependence, a significant role of structural defects or interface disorder (*e.g.* variation of the density of ligands, capping layer, *etc.*).<sup>288,290</sup> Identification of the involved mechanisms, and of a possible intrinsic contribution due to energy redistribution between acoustic modes, is still an open question.

## 7. Conclusions and outlook

With the development of different linear and nonlinear methods during the last 15 years, the optical scattering, absorption and extinction of single nano-objects can be directly addressed. The most commonly used ones exploit far-field techniques, whose limited spatial resolution is circumvented using diluted samples usually prepared by spin coating a colloidal solution, by the lithographic method, or by chemical growth on a substrate. They are based either on linear approaches, monitoring scattering or extinction of an incident light beam by a nano-object (*e.g.*, dark-field or spatial modulation spectroscopy), or on nonlinear ones, mostly third order ones monitoring two beam interactions (*e.g.*, photothermal technique). They now permit detection of single objects, such as metal nanoparticles and nanowires, semiconductor quantum dots or nanowires, or carbon nanotubes, with sizes down to the few

nanometer range. Their scattering, extinction or absorption spectra, and for some methods (*e.g.*, SMS), the amplitude of the corresponding cross-sections, can be determined, yielding a full experimental knowledge of their optical response, complementary to the information obtained from luminescence spectroscopy.

The results of single nano-object spectroscopy are particularly relevant if the morphology of the optically investigated object is determined, permitting precise analysis of its impact on the object optical response. This can be done either optically for simple shapes, or by electron microscopy or atomic force microscopy, comparison between experimental and computed spectra also showing the important influence of the environment (presence of a substrate, particle–substrate interface layer, surface bound molecules, *etc.*). For instance, quantitative agreement, without introducing free parameters, has been obtained for the extinction spectrum and amplitude of a metal nanoparticle only when it is encapsulated to provide it with a controlled environment. Its knowledge or independent determination is thus a major challenge as in the most general situation it has to be modeled by introducing additional adjustable parameters in comparing experimental and theoretical data.

Combination of optical and morphological characterization of the same nano-object constitutes a major advance for fundamental investigations and for applications of nano-systems. One important input is precise determination of the homogeneous linewidth of the optical resonances of an object, yielding new insights into the physical mechanisms at its origin. Investigation of interacting nanoparticles, as in multicomponent nano-objects formed by interacting particles, is also particularly interesting. The results are well described with classical electrodynamics for large particle separation but the quantum regime for sub-nanometer particle distances is still little explored. Coupling optical measurements and full characterization of a single nano-object by 3D electron microscopy or by chemically analytical electron microscopy also opens many new and still little explored possibilities in the case of complex shape or multimaterial objects.

Advanced electron microscopy techniques such as electron energy-loss spectroscopy (EELS) are also very promising for investigation of plasmonic modes. They yield complementary results to those of optical techniques, allowing for instance observation of optically inactive modes, with also the important advantage of intrinsic high spatial resolution permitting spatial mapping of the electromagnetic density of states of a plasmonic mode in and around a nanoparticle.<sup>297</sup> Recently, optical (dark-field microscopy) and electronic (cathodoluminescence and EELS) studies were combined on single gold nano-decahedra, and the measured spectra compared.<sup>298</sup>

Nonlinear extinction and scattering methods were developed to investigate the ultrafast optical response of single nano-objects using femtosecond pump–probe spectroscopy. They actually yield information on its third order nonlinearity in a four-wave mixing type of configuration, which can also be applied to detect the presence of a nano-object as other nonlinear methods as second or third order hyper-Rayleigh scattering. Quantitative information on the optical nonlinearity

of a nano-object has thus been obtained using time-resolved spectroscopy, permitting, in particular, to determine and model the physical mechanisms at the origin of the third order nonlinearity in plasmonic nano-objects. These methods have also been used to investigate energy redistribution processes in a nano-object or to its surrounding or its vibrational response, yielding in particular information on particle–environment coupling. However, as for its linear optical response, understanding of the measured thermal or acoustical energy transfer to the environment requires precise knowledge and modeling of the latter and of the particle–environment interface (e.g., presence and density of ligand molecules, presence and contact with the substrate, oxidation layer), which are still open questions. Conversely, experimental determination of the energy transfer rate could also be exploited to obtain information on the interface, or at least to compare them for different nanoparticle synthesis methods.

## Acknowledgements

The authors would like to thank former PhD students who contributed to single-particle studies, in particular, from the FemtoNanoOptics group: Anna Lombardi, Jean-Christophe Blanc, Vincent Juvé and Hatim Baida.

## References

- 1 A. P. Alivisatos, *Science*, 1996, **271**, 933.
- 2 N. Del Fatti, C. Voisin, F. Chevy, F. Vallée and C. Flytzanis, *J. Chem. Phys.*, 1999, **110**, 11484.
- 3 C. Voisin, N. Del Fatti, D. Christofilos and F. Vallée, *J. Phys. Chem. B*, 2001, **105**, 2264.
- 4 L. H. F. Andrade, A. Laraoui, M. Vomir, D. Muller, J.-P. Stoquert, C. Estournès, E. Beaurepaire and J.-Y. Bigot, *Phys. Rev. Lett.*, 2006, **97**, 127401.
- 5 I. Robel, V. Subramanian, M. Kuno and P. V. Kamat, *J. Am. Chem. Soc.*, 2006, **128**, 2385.
- 6 D. Mongin, E. Shaviv, P. Maioli, A. Crut, U. Banin, N. Del Fatti and F. Vallée, *ACS Nano*, 2012, **6**, 7034.
- 7 C. Voisin, D. Christofilos, N. Del Fatti and F. Vallée, *Phys. B*, 2002, **316–317**, 89.
- 8 V. Juvé, M. Scardamaglia, P. Maioli, A. Crut, S. Merabia, L. Joly, N. Del Fatti and F. Vallée, *Phys. Rev. B: Condens. Matter Mater. Phys.*, 2009, **80**, 195406.
- 9 B. Sharma, R. R. Frontiera, A.-I. Henry, E. Ringe and R. P. Van Duyne, *Mater. Today*, 2012, **15**, 16.
- 10 N. W. Ashcroft and N. D. Mermin, *Solid State Physics*, Saunders College Publishing, 1976.
- 11 J. A. A. J. Perenboom, P. Wyder, L. Festkörperphysik and F. Meier, *Phys. Rep.*, 1981, **78**, 173.
- 12 W. Halperin, *Rev. Mod. Phys.*, 1986, **48**, 533.
- 13 S. Eustis and M. A. El-Sayed, *Chem. Soc. Rev.*, 2006, **35**, 209.
- 14 U. Kreibig and M. Vollmer, *Optical Properties of Metal Clusters*, Springer Verlag, New York, 1995.
- 15 M. Dahan, S. Lévi, C. Luccardini, P. Rostaing, B. Riveau and A. Triller, *Science*, 2003, **302**, 442.
- 16 K. A. Willets and R. P. Van Duyne, *Annu. Rev. Phys. Chem.*, 2007, **58**, 267.
- 17 I. H. El-Sayed, X. Huang and M. A. El-Sayed, *Nano Lett.*, 2005, **5**, 829.
- 18 P. Zijlstra, J. W. M. Chon and M. Gu, *Nature*, 2009, **459**, 410.
- 19 M. Kauranen and A. V. Zayats, *Nat. Photonics*, 2012, **6**, 737.
- 20 H. A. Atwater and A. Polman, *Nat. Mater.*, 2010, **9**, 205.
- 21 M. Hu, X. Wang, G. V. Hartland, P. Mulvaney, J. P. Juste and J. E. Sader, *J. Am. Chem. Soc.*, 2003, **125**, 14925.
- 22 M. Pelton, J. E. Sader, J. Burgin, M. Liu, P. Guyot-Sionnest and D. Gosztola, *Nat. Nanotechnol.*, 2009, **4**, 492.
- 23 F. Wang and Y. R. Shen, *Phys. Rev. Lett.*, 2006, **97**, 206806.
- 24 M. Faraday, *Philos. Trans. R. Soc. London*, 1857, **147**, 145.
- 25 G. Mie, *Ann. Phys.*, 1908, **25**, 377.
- 26 M. Bruchez, M. Moronne, P. Gin, S. Weiss and A. P. Alivisatos, *Science*, 1998, **281**, 2013.
- 27 G. Raschke, S. Kowarik, T. Franzl, C. Sönnichsen, T. A. Klar, J. Feldmann, A. Nichtl and K. Kürzinger, *Nano Lett.*, 2003, **3**, 935.
- 28 S. Kühn, U. Håkanson, L. Rogobete and V. Sandoghdar, *Phys. Rev. Lett.*, 2006, **97**, 017402.
- 29 W. E. Moerner and L. Kador, *Phys. Rev. Lett.*, 1989, **62**, 2535.
- 30 M. Orrit and J. Bernard, *Phys. Rev. Lett.*, 1990, **65**, 2716.
- 31 E. Betzig and R. J. Chichester, *Science*, 1993, **262**, 1422.
- 32 J. J. Macklin, J. K. Trautman, T. D. Harris and L. E. Brus, *Science*, 1996, **272**, 255.
- 33 W. E. Moerner and D. P. Fromm, *Rev. Sci. Instrum.*, 2003, **74**, 3597.
- 34 S. A. Empedocles, D. J. Norris and M. G. Bawendi, *Phys. Rev. Lett.*, 1996, **77**, 3873.
- 35 F. Vietmeyer, M. P. McDonald and M. Kuno, *J. Phys. Chem. C*, 2012, **116**, 12379.
- 36 M. J. O'Connell, S. M. Bachilo, C. B. Huffman, V. C. Moore, M. S. Strano, E. H. Haroz, K. L. Rialon, P. J. Boul, W. H. Noon, C. Kittrell, J. Ma, R. H. Hauge, R. B. Weisman and R. E. Smalley, *Science*, 2002, **297**, 593.
- 37 J. Cui, A. P. Beyler, T. S. Bischof, M. W. B. Wilson and M. G. Bawendi, *Chem. Soc. Rev.*, 2014, **43**, 1287.
- 38 M. Loumagine, A. Richard, J. Laverdant, D. Nutarelli and A. Débarre, *Nano Lett.*, 2010, **10**, 2817.
- 39 H. Wang, T. B. Huff, D. A. Zweifel, W. He, P. S. Low, A. Wei and J.-X. Cheng, *Proc. Natl. Acad. Sci. U. S. A.*, 2005, **102**, 15752.
- 40 M. S. Dresselhaus, G. Dresselhaus, A. Jorio, A. G. Souza Filho and R. Saito, *Carbon*, 2002, **40**, 2043.
- 41 J. Butet, J. Duboisset, G. Bachelier, I. Russier-Antoine, E. Benichou, C. Jonin and P.-F. Brevet, *Nano Lett.*, 2010, **10**, 1717.
- 42 M. Lippitz, M. A. van Dijk and M. Orrit, *Nano Lett.*, 2005, **5**, 799.
- 43 F. Masia, W. Langbein and P. Borri, *Phys. Rev. B: Condens. Matter Mater. Phys.*, 2012, **85**, 235403.







- 193 H. Baida, D. Christofilos, P. Maioli, A. Crut, N. Del Fatti and F. Vallée, *Eur. Phys. J. D.*, 2011, **63**, 293.
- 194 P. Zijlstra, P. M. R. Paulo, K. Yu, Q.-H. Xu and M. Orrit, *Angew. Chem., Int. Ed.*, 2012, **51**, 8352.
- 195 J. A. Scholl, A. L. Koh and J. A. Dionne, *Nature*, 2012, **483**, 421.
- 196 H. Haberland, *Nature*, 2013, **494**, E1.
- 197 A. Wokaun, J. P. Godon and P. F. Liao, *Phys. Rev. Lett.*, 1982, **48**, 957.
- 198 C. Novo, D. Gomez, J. Pérez-Juste, Z. Zhang, H. Petrova, M. Reismann, P. Mulvaney and G. V. Hartland, *Phys. Chem. Chem. Phys.*, 2006, **8**, 3540.
- 199 L. S. Slaughter, W.-S. Chang, P. Swanglap, A. Tcherniak, B. P. Khanal, E. R. Zubarev and S. Link, *J. Phys. Chem. C*, 2010, **114**, 4934.
- 200 E. Shaviv, O. Schubert, M. Alves-Santos, G. Goldoni, R. Di Felice, F. Vallée, N. Del Fatti, U. Banin and C. Sönnichsen, *ACS Nano*, 2011, **5**, 4712.
- 201 E. Hao and G. C. Schatz, *J. Chem. Phys.*, 2004, **120**, 357.
- 202 B. M. Reinhard, M. Siu, H. Agarwal, A. P. Alivisatos and J. Liphardt, *Nano Lett.*, 2005, **5**, 2246.
- 203 N. Grillet, D. Manchon, F. Bertorelle, C. Bonnet, M. Broyer, E. Cottancin, J. Lermé, M. Hillenkamp and M. Pellarin, *ACS Nano*, 2011, **5**, 9450.
- 204 L. V. Brown, H. Sobhani, J. B. Lassiter, P. Nordlander and N. J. Halas, *ACS Nano*, 2010, **4**, 819.
- 205 K.-H. Su, Q.-H. Wei, X. Zhang, J. J. Mock, D. R. Smith and S. Schultz, *Nano Lett.*, 2003, **3**, 1087.
- 206 J. A. Fan, C. Wu, K. Bao, J. Bao, R. Bardhan, N. J. Halas, V. N. Manoharan, P. Nordlander, G. Shvets and F. Capasso, *Science*, 2010, **328**, 1135.
- 207 N. Verellen, Y. Sonnenfraud, H. Sobhani, F. Hao, V. V. Moshchalkov, P. Van Dorpe, P. Nordlander and S. A. Maier, *Nano Lett.*, 2009, **9**, 1663.
- 208 S. Mukherjee, H. Sobhani, J. B. Lassiter, R. Bardhan, P. Nordlander and N. J. Halas, *Nano Lett.*, 2010, **10**, 2694.
- 209 A. S. Urban, X. Shen, Y. Wang, N. Large, H. Wang, M. W. Knight, P. Nordlander, H. Chen and N. J. Halas, *Nano Lett.*, 2013, **13**, 4399.
- 210 P. K. Jain, W. Huang and M. A. El-Sayed, *Nano Lett.*, 2007, **7**, 2080.
- 211 S. Sheikholeslami, Y.-W. Jun, P. K. Jain and A. P. Alivisatos, *Nano Lett.*, 2010, **10**, 2655.
- 212 M. P. Busson, B. Rolly, B. Stout, N. Bonod, E. Larquet, A. Polman and S. Bidault, *Nano Lett.*, 2011, **11**, 5060.
- 213 S. Marhaba, G. Bachelier, C. Bonnet, M. Broyer, E. Cottancin, N. Grillet, J. Lermé, J.-L. Vialle and M. Pellarin, *J. Phys. Chem. C*, 2009, **113**, 4349.
- 214 J. Kern, S. Grossmann, N. V. Tarakina, T. Häckel, M. Emmerling, M. Kamp, J.-S. Huang, P. Biagioni, J. C. Prangsma and B. Hecht, *Nano Lett.*, 2012, **12**, 5504.
- 215 P. K. Jain and M. A. El-Sayed, *Nano Lett.*, 2008, **8**, 4347.
- 216 J. Merlein, M. Kahl, A. Zuschlag, A. Sell, A. Halm, J. Boneberg, P. Leiderer, A. Leitenstorfer and R. Bratschitsch, *Nat. Photonics*, 2008, **2**, 230.
- 217 K. J. Savage, M. M. Hawkeye, R. Esteban, A. G. Borisov, J. Aizpurua and J. J. Baumberg, *Nature*, 2012, **491**, 574.
- 218 R. Esteban, A. G. Borisov, P. Nordlander and J. Aizpurua, *Nat. Commun.*, 2012, **3**, 825.
- 219 J. Zuloaga, E. Prodán and P. Nordlander, *Nano Lett.*, 2009, **9**, 887.
- 220 B. Luk'yanchuk, N. I. Zheludev, S. A. Maier, N. J. Halas, P. Nordlander, H. Giessen and C. T. Chong, *Nat. Mater.*, 2010, **9**, 707.
- 221 G. Bachelier, I. Russier-Antoine, E. Benichou, C. Jonin, N. Del Fatti, F. Vallée and P.-F. Brevet, *Phys. Rev. Lett.*, 2008, **101**, 197401.
- 222 P. Nordlander and E. Prodán, *Nano Lett.*, 2004, **4**, 2209.
- 223 J. J. Mock, R. T. Hill, A. Degiron, S. Zauscher, A. Chilkoti and D. R. Smith, *Nano Lett.*, 2008, **8**, 2245.
- 224 M. Hu, A. Ghoshal, M. Marquez and P. G. Kik, *J. Phys. Chem. C*, 2010, **114**, 7509.
- 225 D. Y. Lei, A. I. Fernández-Domínguez, Y. Sonnenfraud, K. Appavoo, R. F. Haglund, J. B. Pendry and S. A. Maier, *ACS Nano*, 2012, **6**, 1380.
- 226 F. Le, N. Z. Lwin, J. M. Steele, M. Käll, N. J. Halas and P. Nordlander, *Nano Lett.*, 2005, **5**, 2009.
- 227 J. Mertens, A. L. Eiden, D. O. Sigle, F. Huang, A. Lombardo, Z. Sun, R. S. Sundaram, A. Colli, C. Tserkezis, J. Aizpurua, S. Milana, A. C. Ferrari and J. J. Baumberg, *Nano Lett.*, 2013, **13**, 5033.
- 228 H. Baida, A. Crut, P. Maioli, T. B. Nguyen, D. H. Nguyen, N. Del Fatti and F. Vallée, *Adv. Nat. Sci.: Nanosci. Nanotechnol.*, 2011, **2**, 035011.
- 229 M. P. McDonald, F. Vietmeyer and M. Kuno, *J. Phys. Chem. Lett.*, 2012, **3**, 2215.
- 230 A. Shabaev and A. L. Efros, *Nano Lett.*, 2004, **4**, 1821.
- 231 J. Giblin and M. Kuno, *J. Phys. Chem. Lett.*, 2010, **1**, 3340.
- 232 M. Montazeri, A. Wade, M. Fickenscher, H. E. Jackson, L. M. Smith, J. M. Yarrison-Rice, Q. Gao, H. H. Tan and C. Jagadish, *Nano Lett.*, 2011, **11**, 4329.
- 233 A. M. Rao, E. Richter, S. Bandow, B. Chase, P. C. Eklund, K. A. Williams, S. Fang, K. R. Subbaswamy, M. Menon, A. Thess, R. E. Smalley, G. Dresselhaus and M. S. Dresselhaus, *Science*, 1997, **275**, 187.
- 234 J. Lefebvre, D. G. Austing, J. Bond and P. Finnie, *Nano Lett.*, 2006, **6**, 1603.
- 235 P. Avouris, M. Freitag and V. Perebeinos, *Nat. Photonics*, 2008, **2**, 341.
- 236 M. S. Dresselhaus, G. Dresselhaus, A. Jorio, A. G. Souza Filho, M. A. Pimenta and R. Saito, *Acc. Chem. Res.*, 2002, **35**, 1070.
- 237 S. Berciaud, L. Cognet and B. Lounis, *Phys. Rev. Lett.*, 2008, **101**, 077402.
- 238 D. Y. Joh, J. Kinder, L. H. Herman, S.-Y. Ju, M. A. Segal, J. N. Johnson, G. K.-L. Chan and J. Park, *Nat. Nanotechnol.*, 2011, **6**, 51.
- 239 D. Wang, M. T. Carlson and H. H. Richardson, *ACS Nano*, 2011, **5**, 7391.
- 240 Y.-F. Xiao, T. Q. Nhan, M. W. B. Wilson and J. M. Fraser, *Phys. Rev. Lett.*, 2010, **104**, 017401.
- 241 S. Choi, J. Deslippe, R. B. Capaz and S. G. Louie, *Nano Lett.*, 2013, **13**, 54.

- 242 R. R. Nair, P. Blake, A. N. Grigorenko, K. S. Novoselov, T. J. Booth, T. Stauber, N. M. R. Peres and A. K. Geim, *Science*, 2008, **320**, 1308.
- 243 K. F. Mak, M. Y. Sfeir, Y. Wu, C. H. Lui, J. A. Misewich and T. F. Heinz, *Phys. Rev. Lett.*, 2008, **101**, 196405.
- 244 M. Aeschlimann, M. Bauer, D. Bayer, T. Brixner, F. J. García de Abajo, W. Pfeiffer, M. Rohmer, C. Spindler and F. Steeb, *Nature*, 2007, **446**, 301.
- 245 K. F. MacDonald, Z. L. Sámon, M. I. Stockman and N. I. Zheludev, *Nat. Photonics*, 2008, **3**, 55.
- 246 G. L. Eesley, *Phys. Rev. Lett.*, 1983, **51**, 2140.
- 247 C.-K. Sun, F. Vallée, L. H. Acioli, E. P. Ippen and J. G. Fujimoto, *Phys. Rev. B: Condens. Matter Mater. Phys.*, 1994, **50**, 15337.
- 248 N. Del Fatti, R. Bouffanais, F. Vallée and C. Flytzanis, *Phys. Rev. Lett.*, 1998, **81**, 922.
- 249 T. Tokizaki, A. Nakamura, S. Kaneko, K. Uchida, S. Omi, H. Tanji and Y. Asahara, *Appl. Phys. Lett.*, 1994, **65**, 941.
- 250 B. Lamprecht, J. R. Krenn, A. Leitner and F. R. Aussenegg, *Phys. Rev. Lett.*, 1999, **83**, 4421.
- 251 T. Hanke, G. Krauss, D. Träutlein, B. Wild, R. Bratschitsch and A. Leitenstorfer, *Phys. Rev. Lett.*, 2009, **103**, 257404.
- 252 A. Anderson, K. S. Deryckx, X. G. Xu, G. Steinmeyer and M. B. Raschke, *Nano Lett.*, 2010, **10**, 2519.
- 253 N. Del Fatti, C. Flytzanis and F. Vallée, *Appl. Phys. B: Photophys. Laser Chem.*, 1999, **68**, 433.
- 254 V. Juvé, A. Crut, P. Maioli, M. Pellarin, M. Broyer, N. Del Fatti and F. Vallée, *Nano Lett.*, 2010, **10**, 1853.
- 255 J. H. Hodak, A. Henglein and G. V. Hartland, *J. Chem. Phys.*, 1999, **111**, 8613.
- 256 D. G. Cahill, W. K. Ford, K. E. Goodson, G. D. Mahan, A. Majumdar, H. J. Maris, R. Merlin and S. R. Phillpot, *J. Appl. Phys.*, 2003, **93**, 793.
- 257 Y. Matsuo and K. Sasaki, *Jpn. J. Appl. Phys.*, 2001, **40**, 6143.
- 258 N. Del Fatti and F. Vallée, *Appl. Phys. B: Photophys. Laser Chem.*, 2001, **73**, 383.
- 259 M. Montazeri, H. E. Jackson, L. M. Smith, J. M. Yarrison-Rice, J.-H. Kang, Q. Gao, H. H. Tan and C. Jagadish, *Nano Lett.*, 2012, **12**, 5389.
- 260 M. A. Van Dijk, M. Lippitz, D. Stolwijk and M. Orrit, *Opt. Express*, 2007, **15**, 2273.
- 261 F. Vallée and N. Del Fatti, in *Plasmonics in metal nanostructures: Theory and applications*, ed. T. Shahbazyan and M. Stockman, Challenges and Advances in Computational Chemistry and Physics, Springer, 2013.
- 262 N. Del Fatti, A. Arbouet and F. Vallée, *Appl. Phys. B: Photophys. Laser Chem.*, 2006, **84**, 175.
- 263 F. Masia, W. Langbein and P. Borri, *Phys. Chem. Chem. Phys.*, 2013, **15**, 4226.
- 264 C. R. Carey, Y. Yu, M. Kuno and G. V. Hartland, *J. Phys. Chem. C*, 2009, **113**, 19077.
- 265 F. Vielmeyer, P. A. Frantsuzov, B. Janko and M. Kuno, *Phys. Rev. B: Condens. Matter Mater. Phys.*, 2011, **83**, 115319.
- 266 B. Gao, G. V. Hartland and L. Huang, *J. Phys. Chem. Lett.*, 2013, **4**, 3050.
- 267 T. Schumacher, H. Giessen and M. Lippitz, *Nano Lett.*, 2013, **13**, 1706.
- 268 A. Laraoui, V. Halté, M. Vomir, J. Vénuat, M. Albrecht, E. Beaurepaire and J.-Y. Bigot, *Eur. Phys. J. D*, 2007, **43**, 251.
- 269 A. Laraoui, J. Vénuat, V. Halté, M. Albrecht, E. Beaurepaire and J.-Y. Bigot, *J. Appl. Phys.*, 2007, **101**, 09C105.
- 270 H. G. Craighead, *Science*, 2000, **290**, 1532.
- 271 J. Cuffe, O. Ristow, E. Chávez, A. Shchepetov, P.-O. Chapuis, F. Alzina, M. Hettich, M. Prunnila, J. Ahopelto, T. Dekorsy and C. M. Sotomayor Torres, *Phys. Rev. Lett.*, 2013, **110**, 095503.
- 272 J. H. Hodak, I. Martini and G. V. Hartland, *J. Chem. Phys.*, 1998, **108**, 9210.
- 273 E. Duval, A. Boukenter and B. Champagnon, *Phys. Rev. Lett.*, 1986, **56**, 2052.
- 274 H. E. Saucedo, D. Mongin, P. Maioli, A. Crut, M. Pellarin, N. Del Fatti, F. Vallée and I. L. Garzón, *J. Phys. Chem. C*, 2012, **116**, 25147.
- 275 L. Bonacina, A. Callegari, C. Bonati, F. van Mourik and M. Chergui, *Nano Lett.*, 2006, **6**, 7.
- 276 J. Margueritat, J. Gonzalo, C. N. Afonso, A. Mlayah, D. B. Murray and L. Saviot, *Nano Lett.*, 2006, **6**, 2037.
- 277 A. Crut, P. Maioli, N. Del Fatti and F. Vallée, *Phys. Chem. Chem. Phys.*, 2009, **11**, 5882.
- 278 H. Portales, N. Goubet, L. Saviot, S. Adichtchev, D. B. Murray, A. Mermet, E. Duval and M.-P. Pilani, *Proc. Natl. Acad. Sci. U. S. A.*, 2008, **105**, 14784.
- 279 M. F. Cardinal, D. Mongin, A. Crut, P. Maioli, B. Rodríguez-González, J. Pérez-Juste, L. M. Liz-Marzán, N. Del Fatti and F. Vallée, *J. Phys. Chem. Lett.*, 2012, **3**, 613.
- 280 D. Mongin, V. Juvé, P. Maioli, A. Crut, N. Del Fatti, F. Vallée, A. Sánchez-Iglesias, I. Pastoriza-Santos and L. M. Liz-Marzán, *Nano Lett.*, 2011, **11**, 3016.
- 281 A. Crut, V. Juvé, D. Mongin, P. Maioli, N. Del Fatti and F. Vallée, *Phys. Rev. B: Condens. Matter Mater. Phys.*, 2011, **83**, 205430.
- 282 C. Voisin, N. Del Fatti, D. Christofilos and F. Vallée, *Appl. Surf. Sci.*, 2000, **164**, 131.
- 283 M. Perner, S. Gresillon, J. März, G. von Plessen, J. Feldmann, J. Porstendorfer, K.-J. Berg and G. Berg, *Phys. Rev. Lett.*, 2000, **85**, 792.
- 284 A. Gambetta, C. Manzoni, E. Menna, M. Meneghetti, G. Cerullo, G. Lanzani, S. Tretiak, A. Piryatinski, A. Saxena, R. L. Martin and A. R. Bishop, *Nat. Phys.*, 2006, **2**, 515.
- 285 A. Nelet, A. Crut, A. Arbouet, N. Del Fatti, F. Vallée, H. Portalès, L. Saviot and E. Duval, *Appl. Surf. Sci.*, 2004, **226**, 209.
- 286 P. Zijlstra, A. L. Tchebotareva, J. W. M. Chon, M. Gu and M. Orrit, *Nano Lett.*, 2008, **8**, 3493.
- 287 A. L. Tchebotareva, M. A. van Dijk, P. V. Ruijgrok, V. Fokkema, M. H. S. Hesselberth, M. Lippitz and M. Orrit, *ChemPhysChem*, 2009, **10**, 111.
- 288 T. A. Major, A. Crut, B. Gao, S. S. Lo, N. Del Fatti, F. Vallée and G. V. Hartland, *Phys. Chem. Chem. Phys.*, 2013, **15**, 4169.
- 289 H. Baida, D. Christofilos, P. Maioli, A. Crut, N. Del Fatti and F. Vallée, *J. Raman Spectrosc.*, 2011, **42**, 1891.

- 290 P. V. Ruijgrok, P. Zijlstra, A. L. Tchebotareva and M. Orrit, *Nano Lett.*, 2012, **12**, 1063.
- 291 G. V. Hartland, *Annu. Rev. Phys. Chem.*, 2006, **57**, 403.
- 292 L. Saviot, C. H. Netting and D. B. Murray, *J. Phys. Chem. B*, 2007, **111**, 7457.
- 293 V. Dubrovskiy and V. Morochnik, *Izv. Earth Phys.*, 1981, **17**, 494.
- 294 L. Saviot and D. Murray, *Phys. Rev. Lett.*, 2004, **93**, 055506.
- 295 R. Marty, A. Arbouet, C. Girard, A. Mlayah, V. Paillard, V. K. Lin, S. L. Teo and S. Tripathy, *Nano Lett.*, 2011, **11**, 3301.
- 296 K. Yu, P. Zijlstra, J. E. Sader, Q.-H. Xu and M. Orrit, *Nano Lett.*, 2013, **13**, 2710.
- 297 J. Nelayah, M. Kociak, O. Stéphan, F. J. García de Abajo, M. Tencé, L. Henrard, D. Taverna, I. Pastoriza-Santos, L. M. Liz-Marzán and C. Colliex, *Nat. Phys.*, 2007, **3**, 348.
- 298 V. Myroshnychenko, J. Nelayah, G. Adamo, N. Gequet, J. Rodríguez-Fernández, I. Pastoriza-Santos, K. F. MacDonald, L. Henrard, L. M. Liz-Marzán, N. I. Zheludev, M. Kociak and F. J. García de Abajo, *Nano Lett.*, 2012, **12**, 4172.
- 299 L. Cognet, S. Berciaud, D. Lasne and B. Lounis, *Anal. Chem.*, 2008, **80**, 2288.
- 300 B. Dacosta Fernandes, M. Spuch-Calvar, H. Baida, M. Tréguer-Delapierre, J. Oberlé, P. Langot and J. Burgin, *ACS Nano*, 2013, **7**, 7630.